Contrasting styles of post-caldera volcanism along the Main Ethiopian Rift: Implications for contemporary volcanic hazards

Karen Fontijn[1,*], Keri McNamara[2], Amdemichael Zafu Tadesse[3], David M Pyle[1], Firawalin Dessalegn[4], William Hutchison[5], Tamsin A Mather[1], Gezahegn Yirgu[3]

[1]Department of Earth Sciences, University of Oxford, United Kingdom

[2]School of Earth Sciences, University of Bristol, United Kingdom

[3]School of Earth Sciences, Addis Ababa University, Ethiopia

[4] Department of Geology, Wollega University, Ethiopia

[5] School of Earth and Environmental Sciences, University of St. Andrews, United Kingdom

*Corresponding author: Karen.Fontijn@earth.ox.ac.uk, karen.fontijn@gmail.com, Tel +44 1865 272045

Abstract

The Main Ethiopian Rift (MER, ~7-9 °N) is the type example of a magma-assisted continental rift. The rift axis is populated with regularly spaced silicic caldera complexes and central stratovolcanoes, interspersed with large fields of small mafic scoria cones. The recent (latest Pleistocene to Holocene) history of volcanism in the MER is poorly known, and no eruptions have occurred in the living memory of the local population. Assessment of contemporary

volcanic hazards and associated risk is primarily based on the study of the most recent eruptive products, typically those emplaced within the last 10-20 ky. We integrate new and published field observations and geochemical data on tephra deposits from the main Late Quaternary volcanic centres in the central MER to assess contemporary volcanic hazards.

Most central volcanoes in the MER host large mid-Pleistocene calderas, with typical diameters of 5-15 km, and associated ignimbrites of trachyte and peralkaline rhyolite composition. In contrast, post-caldera activity at most centres comprises eruptions of peralkaline rhyolitic magmas as obsidian flows, domes and pumice cones. The frequency and magnitude of events varies between individual volcanoes. Some volcanoes have predominantly erupted obsidian lava flows in their most recent post-caldera stage (Fentale), whereas other have had up to 3 moderate-scale (VEI 3-4) explosive eruptions per millennium (Aluto). At some volcanoes we find evidence for multiple large explosive eruptions (Corbetti, Bora-Baricha, Boset-Bericha) which have deposited several centimetres to metres of pumice and ash in currently densely populated regions. This new overview has important implications when assessing the present-day volcanic hazard in this rapidly developing region.

Key words

Main Ethiopian Rift; volcanic hazards; calderas; peralkaline rhyolite; explosive eruptions

40

41 ## 1. Introduction

42 ### 1a. *Volcanic hazards in East Africa*

43 The East African Rift System (EARS) is the classic example of a continental rift system
44 associated with active volcanism (Ebinger 2005). Magmatic systems along the densely
45 populated EARS remain active, as demonstrated by historical eruptions (Siebert et al. 2010),
46 active degassing (Bluth and Carn 2008; Hutchison et al. 2015; Robertson et al. 2016), recent
47 ground deformation at multiple volcanoes (Biggs et al. 2009, 2011; Hutchison et al. 2016a;
48 Wauthier et al. 2013), seismicity (e.g. Keir et al. 2006; Wilks et al. 2017) and ubiquitous
49 evidence for Late Quaternary explosive eruptions in the form of tephra deposits in
50 terrestrial and lacustrine archives (Barker et al. 2003; Blegen et al. 2015; Chalié and Gasse
51 2002; Fontijn et al. 2010, 2012; Hutchison et al. 2016b; Leat 1984; Le Turdu et al. 1999;
52 Martin-Jones et al. 2017; Pyle 1999; Rapprich et al. 2016; Scott 1980). Detailed volcanic
53 hazard assessments and/or ground-based monitoring efforts are, however, almost non-
54 existent, raising concerns in light of population growth and the rapid expansion of
55 geothermal infrastructure on active volcanoes (Aspinall et al. 2011; USAID 2017). A recent
56 assessment of global volcanic risk identified Africa as a region with high population exposure
57 combined with high vulnerability (Auker et al. 2015).

58 Prior studies at individual rift volcanoes in the EARS suggest late Pleistocene recurrence
59 rate for explosive eruptions of order of 500 – 1000 years at silicic centres such as the
60 trachytic Rungwe and Ngozi volcanoes in southern Tanzania (Fontijn et al. 2010, 2012) and
61 the peralkaline rhyolitic complexes of Aluto (Hutchison et al. 2016b) and Corbetti (Martin-
62 Jones et al. 2017) in Ethiopia. These long repose times and the absence of any memory of

63 past explosive eruptions presents challenges for the communication of volcanic hazards risk,
64 both for local communities and the authorities (e.g. Donovan and Oppenheimer 2018).
65
66 **1b.** ***Recent Volcanism in the Main Ethiopian Rift***
67 The Main Ethiopian Rift (MER) in the northernmost EARS (Fig 1), is a mature continental rift
68 where strain is largely accommodated by magmatic intrusion and localised faulting within
69 axial magmatic segments (Beutel et al. 2010; Casey et al. 2006; Ebinger and Casey 2001;
70 Keranen et al. 2004). This pattern is especially well developed in the northern MER. Rifting
71 initiated around 11 Ma in the northern MER (Wolfenden et al. 2004) and around 5-6 Ma
72 (Bonini et al. 2005) or 8-10 Ma (WoldeGabriel et al. 1990) further south. Around 1.6-2 Ma,
73 the distribution of activity narrowed and active faulting (Wonji Fault Belt, after Mohr 1962)
74 and volcanism focussed within the rift floor, leading to the present-day structure (Boccaletti
75 et al. 1998, 1999; Chernet et al. 1998; Corti 2009; Meyer et al. 1975). There is ongoing
76 debate as to whether this shift in spatial distribution of volcano-tectonic activity results
77 from a change in extension direction from orthogonal to oblique to the rift axis (e.g. Abebe
78 et al. 2005; Boccaletti et al. 1998; Wolfenden et al. 2004), an increasing magmatic control
79 over deformation (Buck 2006; Kendall et al. 2005) or continued oblique extension with pre-
80 existing weaknesses (Corti 2008). The Wonji Fault Belt is an oblique intra-rift normal fault
81 system which largely controls the spatial distribution of basaltic small eruptive centres (Fig
82 1; Abebe et al. 2007; Keir et al. 2015; Mohr 1962; Rooney et al. 2011). In this study we focus
83 on the recent (Late Pleistocene – Holocene) explosive volcanic activity in the central MER
84 (~7-9 °N; ~38.5-40 °E): the regularly spaced silicic (caldera) complexes on the rift axis, and
85 the fields of small eruptive centres of mostly mafic composition (Mohr and Wood 1976;
86 Rooney et al. 2005, 2011; Fig 1). The main centres, from North to South, are Fentale, Kone,

87 Boset-Bericha, Gedemsa, Bora-Baricha, Aluto, Shala and Corbetti (Fig 1; see Supplementary
88 Table 1 for a summary, with synonyms and unique GVP code). Two zones of small eruptive
89 centres, considered to be Late Quaternary, occur off-axis in the Bishoftu (Debre Zeyt) and
90 Butajira areas (Fig 1; Keir et al. 2015; Rooney et al. 2011).

91 The late Quaternary eruption histories of central MER volcanoes are poorly known.
92 Improved knowledge of this volcanic history is however critical to assess contemporary
93 volcanic hazards. Several MER volcanoes are sites of active geothermal energy development
94 (Corbetti, Aluto), with others under exploration (Fentale, Tullu Moye), adding further
95 incentive to understand potential volcanic hazards. Within the study area, three volcanic
96 complexes are considered to have had historical eruptions of basaltic or rhyolitic lava:
97 Fentale (13th century AD and/or ca. 1810 AD; Section 3h), Kone (ca. 1810 AD; Section 3g)
98 and Tullu Moye (possibly late 18th century AD and/or ca. 1900 AD; Section 3d). The presence
99 of volcanic ash layers in lacustrine sediment cores (Chalié and Gasse 2002; Martin-Jones et
100 al. 2017), and pumice deposits on the edifices of Aluto (Hutchison et al. 2016b) and Corbetti
101 (Rapprich et al. 2016) volcanoes suggest the frequent occurrence of explosive eruptions in
102 the region.

103 We present new field observations and geochemical data on the youngest tephra
104 deposits from the main silicic centres of Late Quaternary volcanic activity in the central
105 MER. We review literature data to understand the nature of recent activity at each volcano,
106 and evaluate contemporary volcanic hazards. The scope is deliberately broad and aimed at
107 understanding eruption frequencies and magnitudes along the MER at first order. Our
108 observations show that the most recent stages of post-caldera activity are variable in terms
109 of eruption frequency, magnitude and style, despite the closely similar chemical
110 compositions of the magmas and their tectonic environments.

2. Field observations and geochemistry

Fieldwork along the central MER was carried out in three campaigns between 2015 and 2017. Interbedded sequences of tephra, soil and/or lacustrine deposits were logged and sampled in road cuts and gorges near Corbetti, Aluto, Bora-Baricha, Tullu Moye, Gedemsa, Boset-Bericha and Kone (Fig 1; localities in Supplementary Table 2), augmented with literature data from other MER volcanic centres.

Tephra samples were manually crushed, wet-sieved at 80 µm to remove alteration products, and dried at 50 °C. Remaining ash shards were cold-mounted in pre-drilled EpoFix resin discs, ground down with SiC paper and further polished with diamond paste. We carried out glass major element analyses on polished carbon-coated surfaces by Electron Microprobe Analysis (EMPA) using a 4-spectrometer JEOL JXA-8600 Superprobe at the Research Laboratory for Archaeology and the History of Art, University of Oxford, with an accelerating voltage of 15 kV, a defocused beam of 10 µm, and 6nA beam current. For highly vesicular samples with only small glassy surfaces, the beam size was reduced to 5 µm, and beam current lowered to 4 nA. All elements were counted on-peak for 30 s (Si, Al, Fe, Ti, Mg, Ca, K), except for Na (12 s, and analysed first to minimise alkali loss), P (60 s), Mn and Cl (50 s). Off-peak background counting times were half the peak counting times. Data quality was continuously monitored by secondary glass standards analysed at the start, regularly during (at least after every 30 unknowns) and at the end of each analytical session. Average measured values on secondary standards generally fall within 2 standard deviations of published preferred values (Jochum et al. 2006, 2011). Error bars on the measurements of unknowns were calculated using the relative standard deviation of the measured values on

the standard that is closest in composition to the sample. Thirty individual points were attempted per sample. Analyses were carefully screened to evaluate the potential influence of hidden crystals or voids. Only analyses with totals above 92 wt% were retained, except for samples with analytical totals systematically below 95 wt%, in which case the threshold was lowered to 90 wt%. Analytical totals are generally relatively low, typically 94-95 wt%, which can be ascribed to secondary hydration upon alteration, the presence of dissolved volatiles or other minor elements not analysed for (H_2O, F, Zr; e.g. Neave et al. 2012), and Fe_2O_3 determined as FeO (Pearce et al. 2014). Representative results for each volcanic centre are presented in Table 1; the full dataset including secondary standards is available in Supplementary Tables 3a-b. For ease of comparison, data were normalised to 100 wt% on a volatile-free basis (i.e. also excluding Cl).

3. Results: a survey of post-caldera silicic volcanism along the Main Ethiopian Rift

The new field observations, chemical data and Late Quaternary tephrostratigraphy for the silicic MER volcanoes are presented in Figures 2-13. For each volcanic complex, symbols are colour-coded across the figures showing geographic location, stratigraphy and chemistry. Summaries of the post-caldera eruptive history of each complex are presented in Table 2. Below we present our findings in the context of prior work at each volcano.

3a. Corbetti

The Corbetti complex shows evidence for a three-stage volcanic history, first recognised by Di Paola (1971): effusive shield-building, caldera collapse and, following a hiatus, post-caldera pyroclastic activity. The caldera-forming eruption(s) at Corbetti emplaced at least one unit of welded ignimbrite and associated unwelded pyroclastic deposits (Di Paola 1971;

157 Rapprich et al. 2013; Hutchison et al. 2016c), dated to ca. 0.18 Ma (Table 1; Hutchison et al.
158 2016c; WoldeGabriel et al. 1990).

159 At Corbetti, explosive and effusive eruptions of peralkaline rhyolite built the post-caldera
160 edifices of Artu, Urji (or Wendo Koshe) and Chabbi (Fig 2). Artu is thought to predate both
161 Urji and Chabbi, though no absolute chronological constraints exist (Rapprich et al. 2016).
162 Deposits at the base of Chabbi date to ca. 20 ka (Table 1), suggesting that post-caldera
163 activity at Corbetti has been ongoing since at least the latest Pleistocene.

164 Urji predominantly pumice fall and pyroclastic density current (PDC) deposits. Chabbi
165 mainly comprises obsidian lava flows (Rapprich et al. 2016), many of which were preceded
166 by a pyroclastic component (Mohr 1966; Di Paola 1972).. Rapprich et al. (2016) identify
167 about a dozen events alternating between Urji and Chabbi. The most significant and
168 widespread event is the Wendo Koshe Younger Pumice (WKYP), sourced from Urji, and
169 dated at < 2.3 ka cal BP based on radiocarbon dating of underlying soil (Rapprich et al.
170 2016). Martin-Jones et al. (2017) suggest that WKYP corresponds to a 1.3-1.9 ka cal BP
171 tephra found in sediment cores in Lakes Tilo (Fig 1, 3) and Chamo (170 km SSW of Corbetti),
172 which is surprisingly absent from Lake Hawassa. At least four of Chabbi's obsidian flows
173 post-date WKYP (Rapprich et al. 2016), and the Lake Tilo sediment archive suggests at least
174 one post-WKYP explosive eruption (Fig 3; Martin-Jones et al. 2017). According to Rapprich et
175 al. (2016) the WKYP eruption started with small-scale PDC activity and extrusion of an
176 obsidian lava flow, followed by a sustained explosive eruption that left a distinct pumice
177 lapilli fall deposit with an eastward dispersal pattern, and that can be found well outside the
178 caldera. We find no evidence for obsidian lithics in the WKYP fall deposit, and suggest the
179 obsidian lava flow may post-date the fall deposit.

Glass from Corbetti pumice has a highly uniform pantelleritic composition (Fig 3), and based on major element chemistry alone, Corbetti deposits cannot easily be distinguished. Most of our new correlations between sections are constrained by lateral tracing in the field and depositional characteristics (e.g. lithic content, or characteristic bedding). Road sections within the Corbetti Caldera reveal at least two thick pumice fall deposits separated by multiple smaller-scale fall deposits (Fig 3). Pyroclastic sequences predominantly fall deposits, with light-grey aphyric pumice and populations of dense angular obsidian clasts. Obsidian clasts are virtually absent from the WKYP, which is easily identifiable in road sections N and E of the caldera. Some deposits show systematic rhythmic bedding at cm- to dm-scale, suggesting a pulsating nature of the eruption (Fig S1b; Section 3c). In some places, small-scale PDC deposits form m-scale stacks of low-angle cross-bedded and lenticular-bedded pumice and ash units (Fig S1a). From its stratigraphic position, lateral tracing and depositional characteristics we have identified WKYP in proximal and distal sections, and have updated the dispersal map (Fig 2). The upwind and southern dispersal is poorly constrained but volume estimates using the method of Pyle (1989) suggest a minimum deposit volume of 1.3 km^3, with thicknesses of order of 0.5 m in the town of Shashemene (Fig 2). Another prominent and mostly rhythmically bedded pyroclastic deposit with obsidian clasts covers most of the eastern Urji flanks and underlies the WKYP, and is here called the Bedded Pumice. Both deposits are compositionally identical (Fig 3), but pumice textures and depositional features (massive *vs.* rhythmic bedding, presence *vs.* absence of obsidian) allow the deposits to be distinguished. Lateral tracing of thickness and maximum grain size patterns suggests the Bedded Pumice may be dispersed in a roughly circular pattern around Urji, with rhythmically-bedded packages several meters thick deposited within the caldera (Fig 2). The deposit thins rapidly to the north and south and this is

consistent with its rhythmically bedded nature resulting from pulsating behaviour gradually building a conical deposit. Other pyroclastic units exposed in sections within the caldera are of smaller scale (Fig 3).

Near the southern caldera rim, pyroclastic deposits predating the Bedded Pumice are exposed (e.g. section MER010, Fig 3-4b). The most recent unit exposed here is interpreted as Bedded Pumice because of its homogenous chemical composition as well as the occurrence of small-scale ash-rich PDC deposits covering a thin pumice fall unit, and which are also seen elsewhere. Two thick pumice lapilli breccia deposits underneath show slight compositional differences compared to the intra-caldera deposits, and can be correlated to selected ash layers from sediment cores from nearby lakes (Fig 3). A radiocarbon date on charcoal sampled from the soil underneath the oldest terrestrial deposit (MER010J; Fig 3-4b) is dated at 7.75 ± 0.04 ka cal BP (Table 3). This unit chemically resembles (slightly reduced Al_2O_3) a 6.3-8.7 ka cal BP tephra layer in Lake Tilo (TT-13), as well as the bottommost tephra in a Lake Hawassa core (AWT-7) which was dated at >7.4 ka cal BP (Martin-Jones et al. 2017). A 5.7-6.2 ka cal BP tephra in the Lake Hawassa core shows slightly elevated Al_2O_3 concentrations and can be correlated to a thick pumice fall deposit directly underlying the Bedded Pumice (Fig 3-4b).

From a composite stratigraphy of terrestrial sections we find at least 7 pyroclastic fall deposits separated by palaeosols in the last ca. 7-8 ky, 4 of which are correlated between multiple sections (e.g. MER001 and MER010; Fig 3). This is consistent with the frequency of occurrence of ash layers identified in the sediment cores from lakes Hawassa and Tilo (Martin-Jones et al. 2017; Fig 3). Sediment cores of Lake Garba Guracha, 167 km E of Corbetti in the eastern highlands (Fig 1), reportedly contain 4 tephra layers, ranging from 3

to 15 mm thick, in the last 14 kyrs (Tiercelin et al. 2008). Additional chemical data are required for verification, but the most likely source of these tephras is Corbetti. The combined terrestrial and lacustrine records thus suggest a first-order approximation of 1 explosive eruption per 700-1000 years (Martin-Jones et al. 2017; this study).

Small eruptive centres of unknown age occur immediately southeast of Corbetti, East of Lake Hawassa and North of Corbetti (red triangles on Fig 2). A rhyolitic tuff cone complex with its base ca. 40-50 m above the present-day northern shoreline of Lake Hawassa is partly onlapped by obsidian lava flows from Chabbi and surrounded by lacustrine and alluvial sediments (Rapprich et al. 2013; Fig 2). The morphology of the complex, together with the observed chaotic and heterolithic nature of its proximal deposits, mostly emplaced by PDCs (Ben Clarke, pers. comm.), suggests it may have a phreatomagmatic origin. This would be consistent with its location near the lake (e.g. Belousov and Belousova 2001; Poppe et al. 2016) although more detailed facies analyses are needed to confirm this (e.g. White and Valentine 2016). The cones east of Lake Hawassa, including one near the present-day shoreline in the city of Hawassa (Fig 2), are basaltic, and some are interpreted to have a phreatomagmatic origin (Rapprich et al. 2013). Basaltic scoria cones North of Corbetti seem to have erupted mostly along faults continuing further North to Shala Caldera (Fig 2, 5).

3b. Shala Caldera

The pre-caldera geology of the Shala caldera which contains the 250 m deep Lake Shala (Di Paola 1972) comprises deposits of rhyolitic and trachytic effusive and explosive eruptions, including extensive ignimbrites, pumice flow and pumice fall deposits exposed in the caldera

249 walls. Green-grey welded and unwelded ignimbrite deposits associated with the caldera-
250 forming eruption(s) at Shala are dated at 240 ± 30 ka (bulk K-Ar; Mohr et al. 1980).

251 Post-caldera activity at Shala appears limited, and mostly concentrated at the Tullu Fike
252 pumice dome complex (Fig 2). This lies outside the caldera, and is built on an apron of
253 pumice that is 40 m thick on the northern caldera rim (Mohr et al. 1980; Fig 2). The volume
254 of the Tullu Fike complex is ca. 3 km^3 DRE, an order of magnitude less than the cumulative
255 post-caldera eruptive volumes of neighbouring Corbetti or Aluto (Hutchison et al. 2016c).
256 The age of this post-caldera activity is not known, but Tullu Fike may be the source of
257 pumice deposits interbedded with Late Quaternary lacustrine sediments in the Shala caldera
258 walls (Mohr et al. 1980). It is not known whether any eruptive centres exist within the
259 submerged caldera.

260 A few manifestations of basaltic (post-caldera?) volcanism occur in the form of isolated
261 scoria cones in the north and a maar complex and scoria cones in the south (Mohr et al.
262 1980; Galo Salen unit of Trua et al. 1999; Fig 2). Some of these basaltic centres may be
263 associated with Wonji faults cross-cutting the caldera and the area south of it, and which
264 are in some cases also associated with hot springs (Baumann et al. 1975; Hunt et al. 2017).

265

266 ***3c. Aluto***

267 The long-term magmatic evolution of the Aluto volcanic complex involves a trachytic shield-
268 building phase, culminating in one or two caldera-forming eruptions at ca. 300-320 ka
269 (Hutchison et al. 2016b-c). In at least the last 60 kyrs, post-caldera activity has largely filled
270 in, and almost concealed, the caldera, with the eruption and construction of pumice cones
271 and obsidian domes on the edifice (Fig 6; Hutchison et al. 2015, 2016b).

To the west and south-west of the complex, Late Pleistocene and Holocene pyroclastic deposits occur interbedded with lacustrine deposits related to Pleistocene and Holocene lake level high stands of the Ziway-Shala basin (Benvenuti et al. 2002, 2013; Gasse and Street 1978; Le Turdu et al. 1999). Sediment cores from nearby Lakes Abijata (Abiyata) and Langano, taken 24 km SW and 14 km S of Aluto, respectively (Fig 1), suggest the occurrence of up to 25 distinct ash horizons in the last 12 kyrs (Chalié and Gasse, 2002; Gibert et al. 1999, 2002). Aluto is the most likely source for most of these tephras, suggesting a first-order recurrence of 2-3 explosive eruptions per millennium at Aluto at least since the latest Pleistocene.

Our field observations and sampling at Aluto focused on the young pyroclastic units on the edifice (Fig S1c-d), and those interbedded with lacustrine sediments exposed in deep river gorges mainly to the west of the complex (Fig 5, 4d). These latter sections expose tens of meters thick alternations of up to 20 individual pyroclastic deposits with lacustrine deposits (diatomites) and/or palaeosols (Fig 4c). Where they are interbedded with lacustrine deposits, most of these pyroclastic deposits are dominantly clast-supported and relatively well-sorted pumice lapilli breccias at the bottom, with the appearance of a pumice fall deposit. They typically transgress upwards into a more poorly-sorted facies with more fine ash (and possibly diatomite) in the matrix (Fig 4d). Parallel bedding is common, though some units also display undulated and low-angle cross bedding in the fines-dominated parts. Occasionally matrix-supported deposits of laterally varying thickness (up to 1-2 m) and with scattered subrounded pumice clasts occur, interpreted as PDC deposits. Most deposits are interpreted to be fallout that settled through water, with their top, ash-rich parts resulting from the continued arrival of pyroclastic material deposited in the lake's catchment and remobilised as lahars (e.g. Manville et al. 2009). At ca. 8-10 km distance from the centre of

296 Aluto, the lowermost clast-supported parts of the deposits span thicknesses from a few cm
297 to a few tens of dm, which are typically matched by the thickness of the upper matrix-
298 supported parts.

299 Glass major element analyses of pumice lapilli and ash samples both from the main
300 edifice and individual pyroclastic units interbedded with soils or lacustrine deposits (section
301 A01, Fig 5) from a river gully section to the NW, shows that most pumice deposits have
302 distinct pantelleritic compositions (Fig 6; colour-coded sample localities on Fig 5). The
303 topmost, Qup, was previously tentatively correlated to the abundant young-looking pumice
304 deposits occurring under the topsoil on much of the Aluto edifice (Hutchison et al. 2016b).
305 Its distinct chemical composition however only correlates to a limited number of locations
306 sampled across the edifice and to the west (grey dots on Fig 5, blue ones indicate samples
307 with Qup composition; Fig 6). Rather than being the product of a single Plinian-style
308 eruption, we infer that the previously mapped Qup unit comprises multiple pumice lapilli
309 fall deposits sourced from different vents on the edifice. These deposits are often
310 rhythmically bedded at a dm-scale (Fig S1d), which, together with the variety in chemical
311 composition, is consistent with the presence of multiple pumice cones built up along the
312 trace of the caldera ring fracture (Hutchison et al. 2015). Such pumice cones would locally
313 have deposited thick accumulations of pumice lapilli and localised PDC deposits that
314 overlapped, but were not widely dispersed. This is consistent with the presence of multiple
315 moderate-scale pyroclastic deposits interbedded with the lacustrine sediments West of
316 Aluto (Fig 4c-d, 5, S1c-d). We infer that the “true” Qup deposit, i.e. the youngest unit in
317 section A01, and in section MER060 (Fig 5, S1c) was likely sourced from a pumice cone to
318 the NW of the inferred caldera, and which has a prominent ca. 300 m diameter crater
319 (Hutchison et al. 2016b). Four units underlying Qup in A01 are locally correlated in the

lacustrine and terrestrial sections to the NW of the edifice (Fig 5). Radiocarbon dating on shells incorporated in these pyroclastic and lacustrine deposits suggests the top three larger deposits, A9 (corresponding to Qup), A8 and A7 (Fig 5), to have been emplaced within the last 7,300 years (McNamara et al., unpublished data). A full integration of these sections with lake sediment cores will further improve our understanding of the frequency and magnitude of explosive eruptions at Aluto.

One sample of a 15 cm thick pumice layer with an ash matrix, taken NE of Lake Langano (pink dot on Fig 5) resembles some Corbetti glass compositions (Fig 3, 6). This pumice layer lies between two soil-and-breccia deposits, similar to those interpreted by Benvenuti et al. (2013) as early Holocene shore deposits. Gastropod shells from immediately beneath the pyroclastic unit were dated at 11.97 ± 0.09 ka cal BP (Table 3), and we suggest that this pyroclastic unit may form an early Holocene regional marker horizon from Corbetti.

Numerous scoria cones of basaltic composition have erupted along faults associated with the Wonji Fault Belt which obliquely cross-cuts the rift floor to the East of Aluto but which do not have an obvious physical connection to the complex (Fig 1, 5). With the exception of one trachyandesitic scoria cone to the NW of the complex (TAC in Fig 5) and potentially mafic components in a few (tuff) cones (all of unknown age) in the vicinity of Lake Ziway (TC in Fig 5), no clear manifestation of post-caldera mafic or intermediate volcanism is known at Aluto (Hutchison et al. 2016b; Di Paola 1972).

3d. Bora-Baricha and Tullu Moye

The low-relief complexes of Bora-Baricha and Tullu Moye, between lakes Ziway and Koka (Fig 1, 7) are poorly accessible and the least studied MER volcanoes. Welded pantelleritic

ignimbrites outcrop in the heavily faulted SE of the complex (Trua et al 1999) and have reported ages ranging from 115 ka to 1.8 Ma (fission track and K-Ar; Bigazzi et al. 1993). Remnants of caldera walls may largely be concealed by younger eruptive products. The Bora edifice is highly dissected, whereas Baricha and the Tullu Moye complex both have abundant obsidian lava flows and domes with limited soil cover, as well as hydrothermal manifestations (Fig 7; Admassu Bahiru 2007; Mengistu Darge et al. 2017).

Exploration on western and eastern sides of the complex reveals abundant silicic pyroclastic material in the form of (sometimes crudely parallel-bedded) pumice and ash fall deposits and subordinate PDC deposits. Near Baricha we find an accumulation of > 7 pumice lapilli breccia deposits alternating with poorly-developed palaeosols (section MER147; Fig 7, 8a-b). These deposits are typically characterised by a light grey dominant pumice component and a small proportion of darker grey vesicular pumice and angular obsidian chips. The pumice is a sanidine-phyric pantellerite (Fig 8c). A nearby gully exposes at least 6 more pyroclastic deposits underneath. The age of these deposits is unconstrained due to the lack of dateable material (e.g. charcoal); however the fresh appearance of the pumice and limited soil cover is consistent with a Late Quaternary age.

To the southeast of the complex, section MER150 reveals a stack of > 5 pyroclastic fall and PDC deposits, each unit multiple meters thick, and alternating with poorly-developed soils and reworked yellow ash horizons (Fig 7, 8a-b). The pumice lapilli are light grey and very phenocryst-poor to aphyric, and the deposits generally contain a few % of obsidian lithics as well as some (hydrothermally) altered lithic clasts. Several meters of subparallel cm-scale bedded poorly-sorted deposits of coarse ash, pumice and obsidian show subtle

366 thickness variations and minor cross-bedding in the individual beds, interpreted as dilute
367 PDC deposits. Pumice in all units is pantelleritic, but the top unit (MER150C) is distinctive
368 and may form a fractionation trend towards the Tullu Moye comendites (MER152; Fig 7, 8c).
369 We suspect that the low-relief ridges and domes to the east of Bora, including the Oda
370 crater (Fig 7), were the source of most of the deposits of MER150.

371 Pyroclastic deposits near Tullu Moye are typically poorly-sorted pumice lapilli and bomb
372 breccia deposits, with angular blocks of obsidian (MER152; Fig 8b). The light grey
373 phenocryst-poor pumice has a comenditic glass composition (Fig 8c) and often appears
374 highly altered, with abundant secondary mineralisation. This is consistent with the
375 persistent hydrothermal activity in the region (Mengistu Darge et al. 2017).

376 Poorly-vegetated obsidian lava flows near Tullu Moye (Di Paola 1972; Gouin 1979; Global
377 Volcanism Program, http://volcano.si.edu) occur along fissures with the same strike as faults
378 cutting through basaltic scoria cones further south as well as north towards Gedemsa (Fig
379 7). The youngest (least vegetated) of these obsidian flows erupted from two NNE-SSW
380 aligned vents and formed two highly fractured > 5 m thick lava lobes; one elongate and ca.
381 2.7 km long by 1.6 km wide (also known as “Giano”, Bizouard and Di Paola 1978), and one
382 circular lobe ca. 1 km in diameter (darkest green lobes on Fig 7). The brecciated lava is dark
383 grey to black and phenocryst-poor, with individual blocks showing decimetre-scale vesicular
384 banding. Eyewitness accounts mentioned in Gouin (1979) suggest the eruption took place
385 around 1900 AD and may have been associated with an ash fall. Bizouard and Di Paola
386 (1978) attribute this same lava flow (“Giano”) to an eruption “only two centuries ago”, i.e.
387 late 18th century AD (Siebert et al. 2010; Global Volcanism Program: http://volcano.si.edu).
388 It is possible that both sources in fact refer to the same, poorly dated eruption. Another

young but slightly more vegetated obsidian flow occurs ca. 5 km further SSW (brightest green lobe on Fig 7) and is consistent with two recent eruptions happening in the Tullu Moye area.

3e. Gedemsa

Gedemsa is a ca. 8 km diameter and well-expressed caldera cut by the NNE-SSW trending Wonji Fault Belt along its eastern side (Fig 7). Pre-caldera products exposed on the outer flanks of the complex mostly consist of rhyolitic lava flows and domes, and pumice fall deposits (Thrall 1973; Peccerillo et al. 2003).

Light to dark grey pumice breccia deposits up to 40 m thick are described to the W of the caldera (Thrall 1973). In the north, these coarse pumice deposits alternate at a metre-scale with a few tens of cm thick packages of low-angle cross-bedded pyroclastic deposits from dilute PDCs (Fig 9a). They are overlain by a lower dark and dense, and an upper green and columnar-jointed welded ignimbrite (Thrall 1973). The green welded ignimbrite is overlain by pumice breccia deposits up to 20 m thick (Thrall 1973). The ignimbrites are typically associated to one or more caldera-forming events (Peccerillo et al. 2003), but given the volume of the underlying sequence of major unconsolidated pyroclastic deposits, including coarse pumice lapilli breccias, we suspect these latter deposits may also be related to the formation of the caldera. K-Ar dating on crystal separates of unidentified pre- and post-caldera products constrains the formation of the caldera to within 265 ± 0.02 and 319 ± 0.02 ka (Peccerillo et al. 2003). Morton et al. (1979) however present a bulk K-Ar age of 0.85 ± 0.07 Ma for a green welded tuff on the N rim of the Gedemsa caldera.

411 Light to dark grey pumice breccia banked up against green welded ignimbrites in the
412 southern caldera wall (MER076A/B; Fig 7) correspond chemically to a grey pumice lapilli
413 breccia deposit on the eastern flank of the complex (MER094A; Fig 7, 9d-e). Another poorly-
414 sorted dark grey pumice lapilli fall deposit underlies welded ignimbrites in the NE caldera
415 rim and on the NE flank (MER084A; Fig 7, 9a), and corresponds chemically to pyroclastic
416 deposits exposed in a river gully to the east (MER077A/B; Fig 7, 9d-e). Here, crudely bedded
417 dark grey fine pumice lapilli breccia interpreted as a fall deposit, is overlain by a poorly-
418 sorted matrix-supported deposit with dispersed clasts of light grey fibrous pumice lapilli.
419 This deposit gradually transgresses upwards into a welded facies, and is interpreted as a
420 PDC deposit. Both deposits are separated by an ash- and lithic-rich soil suggesting a
421 temporal hiatus. The similar chemical composition and widespread nature of the deposits
422 however is consistent with both events being related to caldera-forming eruptions which
423 were relatively closely spaced in time in the Late Quaternary.

424 Three intra-caldera coalesced domes, Kelo, Dima and Kore, are aligned WNW-ESE (Fig 7;
425 Acocella et al. 2002) and mostly comprise poorly-sorted pumice lapilli and bomb breccias,
426 interpreted as proximal fall deposits from the domes (Fig 9b). Kore, the easternmost centre
427 on this alignment, has a prominent ca. 600 m diameter summit crater. Interbedded locally
428 welded facies and obsidian lavas also occur within the deposits of these domes (Thrall 1973;
429 Giordano et al. 2014). Several low-relief dome-shaped constructs are also identified in the
430 northern and southern half of the caldera (Fig 7) and presumably also represent post-
431 caldera centres of activity, though their interpretation as an eruptive volcanic feature is
432 ambiguous.

433 Our sampling revealed at least 6 different pumice lapilli fall deposits that are
434 geochemically distinct from the caldera-forming pyroclastic deposits (Fig 9d-e). Three of
435 these were sampled from the proximal deposits of the intra-caldera Kore, Dima and Kelo
436 edifices and are all pantelleritic in composition (Post-caldera cluster in Fig 9d-e). Three more
437 geochemically unique pumice lapilli fall deposits from sections near the NE rim and E of the
438 caldera presumably relate to additional post-caldera silicic activity, the source vents of
439 which are however not constrained (Fig 7, 9d-e). Thicknesses of these deposits in these
440 localities are of order of a few tens of cm.

441 Near the NE caldera rim, subparallel and low-angle cross-bedded poorly-sorted deposits
442 with up to 10-15 cm clasts of scoria, basaltic lava and obsidian in an ash-rich matrix occur
443 stratigraphically above the post-caldera pumice fall deposits (MER081A; Fig 9c-e). They are
444 interpreted as deposits of dilute PDCs, possibly phreatomagmatic in origin. Peccerillo et al.
445 (2003) relate them to the basaltic volcanism along the Wonji Fault Belt, with evidence for
446 entrapment of intrusive silicic magmas from the crystallising post-caldera Gedemsa
447 reservoir. The exact age of this activity is unknown.

448 Basaltic scoria cones (Peccerillo et al. 2003; Rooney et al. 2007) occur immediately NE, E
449 and S(E) of the complex, aligned with the Wonji Faults (Fig 7). These cones lack silicic
450 enclaves (Peccerillo et al. 2003) and are considered structurally unrelated to Gedemsa.

451 Immediately NW and SW of Gedemsa caldera, Thrall (1973) describes pantelleritic lava
452 domes and local pumice deposits cut by morphologically young faults (Fig 7). It is not known
453 whether these belong to the pre- or post-caldera stage of volcanism of the Gedemsa
454 complex. The same faults control the location of hydrothermal springs a few km further
455 north (Abdulkadir and Eritro 2017).

456

457 ***3f. Boset***

458 Midway between Gedemsa and Boset lies the Melkassa (also known as Sodore) field of ca.
459 30 scoria cones around the largely eroded ca. 5 km diameter Boku caldera (Fig 10). An
460 obsidian lava flow from this caldera was dated by Morton et al. (1979) at 0.83 ± 0.02 Ma
461 (bulk K-Ar). The Melkassa scoria cones and associated lava flows are morphologically young
462 and suspected to be of Late Pleistocene – Holocene age (Boccaletti et al. 1998, 1999; Siebert
463 et al. 2010).

464 The Boset volcanic complex comprises two adjoining stratovolcanoes that grew along a
465 NNE-SSE trending lineament parallel to the Wonji Fault Belt. The southern and largest of the
466 two volcanoes is called Boset-Gudda (also "Tiliki Boset" or "Great Boset"), the northern one
467 Boset-Bericha (also "Tinishi Boset" or "Little Boset"; Fig 10). Gudda has a 2.5 km arcuate
468 ridge on its NW slope, which may represent the remnant of a largely infilled caldera (Di
469 Paola 1972). In a study of the long-term evolution of the Boset volcanic complex constrained
470 by absolute lava flow Ar-Ar chronology, Siegburg et al. (2018) constrain the caldera
471 formation to after 119.8 ± 6.1 ka. We identified a >3.5 m thick stack of altered coarse
472 pumice lapilli breccia and finely parallel and cross-bedded ash and small pumice lapilli
473 deposits of dilute PDCs interbedded with palaeosols on the SE lower flank of the complex,
474 and underneath a lava flow (outcrop MER120, Fig 10). These deposits are pantelleritic in
475 composition, but different from the more recent pyroclastic units to the West (Fig 11). We
476 infer the former to relate to the "ashy and pumiceous falls" described by Ronga et al. (2010)
477 for the late-stage pre-caldera or syn-caldera activity. More dedicated studies are needed to

478 infer where these deposits sit in the long-term stratigraphy of the complex, and whether or
479 not they relate to caldera-forming events.

480 The two central edifices of the complex mainly comprise thick trachytic and peralkaline
481 rhyolite lava flows with associated pyroclastic deposits (Macdonald et al. 2012). These silicic
482 lava flows have run-out distances of up to 11 km (Siegburg et al. 2018) and are often
483 sourced from breached cones. The summit of Gudda contains a handful of NE-SW aligned
484 small craters, up to 200-300 m diameter (blue stars on Fig 10), some with associated short
485 obsidian lava flows (Di Paola 1972) of Holocene age (3.3 ± 2.4 ka, Ar-Ar on feldspar
486 separates, Phase O of Siegburg et al. 2018).

487 Road and dry river gully sections on the Western lower flank of Boset (Fig 10) expose
488 alternations of palaeosols and up to 6 individual pyroclastic deposits, interpreted as fall
489 deposits, one of which is scoriaceous (Fig 11). We propose section MER108 (Fig 10-11) as
490 the type section for the young tephrostratigraphy at Boset.

491 The most recent deposit is also the most voluminous and widespread, and is here called
492 the “Boset Pumice”. It comprises well-sorted pumice lapilli breccia deposits with a minor
493 fraction of small obsidian chips, and is interpreted as a Plinian-style fall deposit. Pumice
494 lapilli are white to light grey, very crystal-poor and have a uniform pantelleritic glass
495 composition (Fig 11). The deposits are crudely parallel-bedded in the most proximal
496 outcrops, where they reach thicknesses of more than 3 m and are commercially exploited.
497 The westward distribution suggests a primary depositional thickness of order of 20 cm in the
498 city of Adama (Fig 10). The northern and eastern (upwind) dispersal are poorly constrained
499 but visits to outcrops along the lower Boset flanks suggest absence of the Boset Pumice
500 deposit in these areas. A first-order approximate volume calculation using the method of

501 Pyle (1989) suggests a minimum deposit volume of 0.5 km^3, corresponding to a sub-Plinian
502 eruption. From the general dispersal pattern we infer that the source vent was located on
503 the Gudda edifice, and it may correspond to one of the craters identified as part of the
504 youngest, Late Holocene, phase of activity at Gudda by Siegburg et al. (2018).

505 Recent basaltic trachyandesitic (mugearitic) lava flows were erupted from the saddle
506 between the rhyolitic Gudda and Bericha edifices (Di Paola 1972; Brotzu et al 1974; Siegburg
507 et al. 2018). Their whole rock composition (Brotzu et al. 1974) is very similar to that of a thin
508 scoria fall deposit which is traceable over more than 10 km (scoria unit #2, found in MER095
509 and in type section MER108; Fig 10-11) and we therefore suspect the latter corresponds to
510 an explosive phase of these mostly effusive eruptions. This is also consistent with the
511 Holocene age (4.2 ± 3.2 ka, Ar-Ar dating on feldspar separates) constrained for one of the
512 lava flows (Fig 10; Siegburg et al. 2018). Several scoria cones of basaltic composition occur
513 along the NE lower flanks of the complex, and are mostly aligned NE-SW (Fig 10).
514 Geochemical analysis on a selection of these scoria cones shows them to have similar
515 basaltic compositions (MER109A, MER116A and MER117A; Fig 10), distinct from our scoria
516 #2 (Fig 11). Other scoria cones occur to the SW of the complex, and are associated with the
517 Melkassa volcanic field (Fig 10).

518 The basaltic trachyandesite scoria fall deposit directly overlies a lithic-poor and crystal-
519 poor pumice fall deposit, and is intermixed in one outcrop. Both eruptions may therefore
520 have occurred almost simultaneously. The second pumice lapilli fall (#3 in Fig 11) is
521 markedly thinner and less widespread than the Boset Pumice, but has a similar pantelleritic
522 composition, and is therefore likely to be sourced from Gudda (Siegburg et al. 2018). A third
523 pantelleritic pumice fall deposit occurs underneath pumice #3. It is normally graded and

finer grained than the Boset Pumice (pumice unit #4; Fig 11). Finally, at the base of the type section MER108 (Fig 10) is a lithic-poor white pumice lapilli deposit with a distinct comenditic glass composition (Fig 11). In one section NW of the complex (MER115, Fig 10), another comenditic pumice lapilli fall deposit occurs underneath pumice #5, separated by a soil. Comenditic lava flows are only known from the Bericha edifice of the Boset complex (Siegburg et al. 2018), so we infer these lowermost comenditic pumice fall deposits to have derived from Bericha. The most recent lava flows at Bericha date to the latest Pleistocene and Holocene (Siegburg et al. 2018) and some may be associated with the comenditic pumice fall deposits.

3g. Kone

The Kone (Gariboldi in older literature) volcanic complex comprises at least three well-expressed nested calderas (Fig 12): the oldest, partially obscured Birenti Caldera which may include two nested collapse features (Cole 1969), the younger Kone Caldera and the Korke embayment (Rampey et al. 2010).

Pre-caldera activity at Birenti and Kone mostly comprises trachyte and alkali rhyolite lava flows and domes exposed in the caldera walls (Rampey et al. 2010). The caldera-forming eruptions emplaced up to several meters or tens of meters of unwelded pumice fall deposits interbedded with welded ignimbrites, typically green in colour and with varying proportions of fiamme and accidental lithics (Rampey et al. 2010). We sampled a sequence of unwelded, coarse grey pumice lapilli and bomb breccia deposits along the road between the Kone and Birenti calderas (Fig 12). We interpret these pyroclastic fall deposits as related to some of

547 the major events described by Rampey et al. (2010). Major element glass chemistry suggests
548 three distinct comenditic to pantelleritic compositions (Fig 13). We infer the comenditic
549 pumice, sampled from three localities along the N rim of the Korke embayment, to be
550 associated with the Kone caldera forming event(s) (unit Qpk, after Rampey et al. 2010). The
551 pantelleritic pumice may represent other units within the Kone pyroclastic sequence, or
552 other phases from the Kone Caldera Complex. MER141A (yellow symbols in Fig 12-13) may
553 correspond to a non-welded pyroclastic facies of the Birenti caldera-forming events (units
554 Qub or Qim, Rampey et al. 2010). MER130A (blue symbols in Fig 12-13), a poorly-sorted,
555 >2.5 m thick grey coarse pumice lapilli and bomb breccia deposit, may correspond to the
556 pyroclastic deposits associated with a post-caldera rhyolitic dome on the southern Kone
557 caldera wall (units Qrd and Qpd, Rampey et al. 2010).

558 The age and detailed stratigraphy of these events remains poorly constrained, and it is
559 unclear which eruption formed the Korke embayment (Rampey et al. 2010). Williams et al.
560 (2004) show a schematic section near the SE margin of the Kone caldera, where a welded
561 ignimbrite and overlying ash (flow?) and pumice fall deposits lie beneath a Middle Stone
562 Age palaeosol (> 200 ka; Basell 2008; Williams et al. 2004). Without additional spatial and
563 geochemical data it is not possible to assign a correlation with any of the pyroclastic
564 deposits described by Rampey et al. (2010).

565 In a study of Middle Stone Age obsidian tool provenance, potential obsidian source rocks
566 sampled near the NE rim of the Kone caldera were Ar-Ar–dated at 391 ± 2 and 395 ± 6 ka
567 (Vogel et al. 2006). Glass geochemical data on these same black to deep green obsidian
568 source rocks (Negash et al. 2007) are closely similar to MER141A (yellow symbols in Fig 12-
569 13), and may put a temporal constraint on the formation of these deposits.

570 Rampey et al. (2010) describe the few post-caldera silicic lava flows and domes which
571 erupted along the southern and northern Kone caldera rims, and along NE-SW oriented
572 faults north of the complex. Sparse pyroclastic deposits are also associated with the caldera
573 ring fault (and may correspond to MER130A, blue symbols in Fig 12-13, see above), but the
574 age of these eruptions is unconstrained, and it is unclear whether they are representative of
575 the contemporary volcanism at the Kone Caldera complex. In our reconnaissance visit we
576 did not find any evidence for fresh-looking loose pyroclastic deposits of silicic composition.

577 Recent basaltic lava flows erupted from NE-SW aligned scoria cones on the hinge
578 between the Kone and Korke calderas, filling both caldera floors (Acocella et al. 2002). The
579 most recent of these events may have occurred historically, with many secondary sources
580 suggesting an eruption date of ca. 1810-1830 AD (e.g. Buxton 1949; Cole 1969), originally
581 derived from the accounts of Harris (1844). In April 1842, Harris visited the "crater of Saboo"
582 (Sabober, S of Fentale; Fig 12), which was "said to have been in full activity in the time of
583 Sahela Selassie's grandsire" (Harris 1844, p. 255). Selassie's grandfather, Asfaw Wossen, was
584 ruler of Shoa from 1774-1808 (Keynes 2007). Harris also visited Kone, which he describes as
585 "the crater of Winzegoor", and where he noted that the fresh lavas were still "jet black",
586 and that two "bare truncated cones" erupted "some thirty years previously" remained dark
587 and cindery. One reading of Harris' accounts is that there was an episode of mafic rift-floor
588 volcanism extending between Kone and Fentale, similar to the Dabbahu – Manda Hararo
589 rifting episode from 2005-2010 (e.g. Ferguson et al. 2010), and that this had a peak in the
590 later parts of Asfaw Wossen's reign, perhaps ca. 1800-1808. Other morphologically fresh
591 and poorly vegetated, blocky basaltic lava flows occur to the N and NE of the caldera
592 complex, most notably to the N of a large scoria cone, Beru (Fig 13). Our glass geochemical
593 analyses confirm the basaltic composition for these recent scoria cones (Fig 12-13).

3h. Fentale

Fentale is the northernmost MER volcano, at the junction with the Afar depression, and hosts a ca. 2.5 by 4 km diameter summit caldera elongated NNW-SSE (Fig 12). The green welded ash-flow tuff of Fentale that was emplaced by the caldera-forming eruption is dated at 168 ± 38 ka by fission track dating on the glass (Williams et al. 2004). Based on the chemical composition of different flow units identified within the ash-flow tuff, Gibson (1974) suggested the related eruption emptied a chemically zoned magma chamber with a trachytic base and rhyolitic top. On the southern flank, the welded tuff deposit has distinctive blisters, sometimes up to 100 m in diameter, presumably formed by degassing of large coalesced gas pockets within the newly emplaced deposit (Gibson 1970).

Post-caldera eruptions of obsidian and rhyolite lava flows were sourced from NNW-SSE aligned vents and fissures within the caldera (Acocella et al. 2002), as well as on the NE, E, SE and W flanks of the volcano (Williams et al. 2004; Gibson 1974). The morphologically youngest and most poorly vegetated obsidian flow was erupted from a vent within the caldera. Some post-caldera eruptions emplacing obsidian lava flows possibly also had an explosive phase, as evident from fresh superficial pumice lapilli scattered around the lower slopes of Fentale. There is however no evidence for significant silicic explosive volcanism emplacing widespread pumice fall deposits in the post-caldera stage at Fentale.

Basaltic activity near Fentale occurs immediately South of the edifice. A basaltic tuff cone, Tinish Sabober (Williams et al. 2004; Fig 12) is covered on its flanks with a veneer of welded tuff from the caldera-forming eruption, hence pre-dates it (Gibson 1967, 1974). Much more recent basaltic activity has occurred in the same region with the emission of

617 lava flows from fissures and small cones aligned NE-SW with the centre of the tuff cone
618 (Williams et al. 2004). Local oral tradition reported by Harris (1844, p255) suggests activity
619 during the reign of Asfaw Wossen, who died in 1808 (Keynes 2007; Section 3g). The fresh
620 and almost non-vegetated nature of the Fentale basaltic lava flows, similar to those at the
621 Kone caldera complex, does suggest they may have erupted historically.

622 A poorly documented "13th century" eruption of Fentale is reported in Newhall and
623 Dzurisin (1988), after Azais and Chambord (1931), who record an account by a priest
624 mentioning the destruction of a church and town near present-day Lake Metehara (also
625 known as Lake Beseka, Fig 12). It is unclear whether this event could actually relate to the
626 19th century lava flows, given their geographic location close to the lake, or whether it
627 represents an eruption from a vent elsewhere on the edifice.

628

629

630 ***3i. Off-axis volcanism***

631 Our evaluation of recent volcanism in the MER is focussed on the on-axis volcanic centres
632 within the MER, which are generally assumed to be the locus of most of the present-day
633 volcanic and tectonic activity (e.g. Corti 2009; Keir et al. 2015). Off-axis volcanism occurs as
634 small eruptive centres of mainly basaltic composition in the Bishoftu (Debre Zeyt) and
635 Butajira volcanic fields on the Western rift shoulder (Fig 1; Rooney et al. 2005, 2011). In the
636 Bishoftu area several phreatomagmatic vents (maars) exist and these comprise pumiceous
637 tuff deposits (Emilia et al. 1977). This off-axis volcanism is generally assumed to be Late
638 Quaternary in age because of its morphologically young appearance, though absolute
639 chronologies or modern evaluations of their potential future hazards are lacking. To the

640 southern end of the Bishoftu area, the large silicic volcano of Ziquala (Zuquala) dominates
641 the landscape, and has a prominent summit crater hosting a lake. Trachytic lavas from the
642 base, flank and rim of the volcano were dated (K-Ar on feldspar separates) between 0.85 ±
643 0.05 and 1.28 ± 0.15 Ma (Morton et al. 1979) but its youngest eruptive products have not
644 been studied.

645

646 **4. Discussion**

647 ***4a. Diversity in style and rate of silicic volcanism along the MER***

648 The timing of caldera-forming eruptions and initiation of post-caldera activity along the MER
649 is still relatively poorly constrained, with the exception of recently re-evaluated ages at
650 Aluto and Corbetti using high-precision sanidine Ar-Ar dating as opposed to bulk K-Ar dating
651 (Hutchison et al. 2016c). In this study we focus mainly on the youngest post-caldera activity
652 at each MER centre as constrained by field observations. Post-caldera Late Quaternary
653 activity along the MER is dominated by effusive and/or explosive eruptions of peralkaline
654 rhyolitic magmas, generating obsidian flows and domes and pumice cones within the old
655 calderas, at all centres except Kone (Table 2).

656 Corbetti and Aluto have both been highly active in the Late Quaternary, as evidenced by
657 the presence of numerous volcanic ash layers in lacustrine sediment cores spanning the last
658 12,000 years (Chalié and Gasse 2002; Martin-Jones et al. 2017), and multiple pumice fall
659 deposits on their edifices. Deposits of these explosive eruptions are moderately widespread,
660 with some suggesting up to sub-Plinian scale magnitudes (typically VEI 3-4, which would
661 correspond to deposit volumes of order of 0.1 km^3; Newhall and Self 1982; Pyle 2015, 2016).
662 The best documented and youngest deposit in our record from Aluto presented here, Qup,

663 is almost 3 meters thick near its presumed source vent, but rapidly thins away to a few tens
664 of cm or even less within 5 km distance both to the W and E (Fig 5). Deposits of similar scale
665 are also found at Tullu Moye and Boset-Bericha. At Gedemsa and possibly also at Tullu Fike
666 near the Shala Caldera, we find more localised coarse pumice bomb breccia deposits
667 representing post-caldera stage explosive activity (Table 2).

668 The metre- to decimetre-thick proximal pyroclastic fall deposits found at Corbetti, Bora-
669 Baricha and Boset-Bericha are consistent with larger, VEI 4-5 eruptions generating deposit
670 volumes of ca. 1 km^3 (Newhall and Self 1982; Pyle 2015, 2016). At Corbetti there is evidence
671 for two such Holocene events, in addition to multiple smaller-scale explosive eruptions (Fig
672 3), some of them possibly associated with the effusion of obsidian lava flows. Proximal-
673 medial multiple-metre thicknesses of pumice fall deposits from Bora and/or Baricha are also
674 consistent with eruptions up to VEI 5. Limited accessibility prevents us from obtaining more
675 detailed magnitude estimates for the scale of these important eruptions. The most
676 prominent recent explosive eruption of the Boset-Bericha complex was that of the sub-
677 Plinian "Boset Pumice".

678 Conservative estimates of VEI 3-4 eruptions and corresponding minimum deposit
679 volumes of 0.01 km^3 and 0.1 km^3 (Pyle 2015, 2016) allow us to semi-quantitatively constrain
680 first-order eruptive rates in the Holocene for some MER volcanoes. Based on the rapid
681 thinning trends of Qup (Fig 5; see above) we assign a magnitude of 3 to all of the 25 Aluto
682 deposits in the last 12,000 years (Table 2) and a magnitude of 4 to 4 of the 7, and magnitude
683 3 to the 3 remaining, Corbetti eruptions constrained on land (based on relative thicknesses
684 in the proximal sections; Fig 3). This results in a minimum estimate of volumetric eruptive
685 rates of 0.01 – 0.1 km^3 / ky at these two volcanoes (assuming 800 kg/m^3 of deposit density,

686 and 2380 kg/m^3 peralkaline rhyolite density, in the absence of other constraints from e.g.
687 water content; Neave et al. 2012), substantially less than the 0.5 – 0.75 km^3 / ky constrained
688 for the mid-Pleistocene "silicic flare-up" in the CMER (primarily Aluto and Corbetti), the
689 period during which most of the calderas were formed (Hutchison et al. 2016c). These
690 modern eruptive rates are also lower but broadly comparable with those estimated for the
691 highly explosive trachytic Rungwe and Ngozi volcanoes in southern Tanzania (ca. 0.25 km^3 /
692 ky; Fontijn et al. 2010, 2012). Note that the above estimates (except for the "flare-up" ones
693 of Hutchison et al. 2016c) do not take into account the effusive eruptive products and are
694 based on minimum eruptive volumes, therefore represent minimum rates.

695 At Aluto and Corbetti most of the obsidian lava flows and *coulées* are presumably
696 associated with an explosive eruption either preceding or following the effusive phase
697 (Hutchison et al. 2016b; Di Paola 1972). This is consistent with the ubiquitous presence of
698 pumice deposits on both edifices, and is observed on other peralkaline volcanoes producing
699 pumice cones and obsidian lavas (Dellino and La Volpe 1995; Mahood and Hildreth 1986).
700 Further north along the MER, at Tullu Moye, but particularly Boset-Bericha and Fentale
701 there is a generally increasing proportion of silicic effusive (obsidian lava flows) over
702 explosive volcanism. At Tullu Moye several of the most recent silicic eruptions have been
703 effusive and emplaced thick obsidian lava flows. We did not encounter evidence of an
704 associated explosive eruption, though the historical accounts of the youngest eruption do
705 suggest the occurrence of ash fall (Gouin 1979). The strongly fault-controlled Boset-Bericha
706 complex has experienced both effusive and a limited number of explosive eruptions in its
707 most recent phases, with most of the edifices built up by silicic lava flows (Fig 10; Siegburg
708 et al. 2018). At Fentale, silicic post-caldera volcanism seems dominated by obsidian lava
709 flows, possibly with a small component of associated explosive activity.

4b. Volcano-tectonic interactions and mafic volcanism along the MER

Active faults of the Wonji Fault Belt cross-cutting Fentale, Kone and Gedemsa facilitate the eruption of basaltic magmas, forming scoria cones and lava flows. At Kone, post-caldera activity is entirely dominated by such small-scale basaltic lava flows and scoria-cone-building eruptions and no silicic products are identified in the post-caldera stage. Also at Gedemsa, the youthful nature of the faults cross-cutting the eastern sector of the caldera, and their aligned scoria cones (Fig 7), are indicative of a predominance of basaltic volcanism over silicic volcanism in the present stage. It has been suggested that the post-caldera basaltic products at these three volcanic complexes should not be considered as part of their respective predominantly silicic complexes, but represent a renewed phase of basaltic activity purely related to the Wonji Fault Belt (Giordano et al. 2014; Gibson 1974).

At Tullu Moye and Boset-Bericha, the Wonji Fault Belt however controls the eruption of both mafic and silicic magmas, which have clearly erupted contemporaneously in the recent past (Fig 7, 10-11; Siegburg et al. 2018). The southernmost clear surface expression of the Wonji Fault Belt is the field of basaltic scoria cones east of Lake Ziway (Fig 1). Whereas this basaltic volcanism is generally assumed to be cogenetic with the silicic products erupted from the post-caldera edifice of Aluto (Hutchison et al. 2016b), the detailed spatial and temporal relationships are not well constrained.

At Aluto and Corbetti all the basaltic (and presumably post-caldera) surface manifestations of volcanism occur well outside the known extent of the calderas and this may reflect the presence of a higher proportion of silicic melt in the crust relative to some of the other systems where basalt erupts along fractures cross-cutting the calderas (Kone,

733 Gedemsa). The larger amounts of silicic crustal melt would in this case prevent the denser
734 basaltic melt to rise up through the caldera and instead deflect it to a “shadow zone”
735 outside the caldera (e.g. Hutchison et al. 2016a; Mahood 1984; Mahood and Hildreth 1986;
736 Jeffery et al. 2016).

737

738 ***4c. Implications for volcanic hazards***

739 Our tephrostratigraphic records for Aluto and Corbetti provide evidence for explosive
740 eruptions at these volcanoes in the Holocene of up to 1-3 explosive events per millennium.
741 Most of these eruptions have been of moderate scale but especially at Corbetti, some
742 appear to be VEI 4-5. The largest Holocene explosive eruptions in the MER deposited several
743 tens of centimetres of pumice and ash in areas which today are densely populated rural
744 areas or urbanised population centres. The Boset Pumice eruption generated a pumice fall
745 deposit of >0.5 km^3, with a deposit thickness of ca. 20 cm in the city of Adama. The most
746 recent large eruption at Corbetti (WKYP) shows a Plinian-style elliptical dispersal pattern,
747 with a dispersal axis to the E and deposition of ca. 50 cm of pumice fall in the town of
748 Shashemene and possibly more than 10 cm in the city of Hawassa (Fig 2). Such deposit
749 thicknesses are sufficient to cause widespread damage and disruption to infrastructure and
750 agriculture (e.g. Ayris and Delmelle 2012; Wilson et al. 2012). The dispersal axes as
751 constrained from these deposits are not all consistent with the present-day dominant wind
752 directions at this latitude (very minor to the SW or NE) but this may be due to the close
753 proximity to the Intertropical Convergence Zone and its possible shifts throughout the Late
754 Quaternary (e.g. Gasse 2000; Lézine et al. 2017).

755 The Bedded Pumice deposit of a large explosive eruption of Corbetti preceding WKYP has
756 entirely overlapping major element composition (Fig 3), and shows rapid thinning away
757 from the vent (i.e. more cone-like deposition, in contrast to sheet-like for WKYP; Fig 2). This
758 is consistent with the rhythmically-bedded nature of its proximal deposits, which have built
759 up a pumice cone (Fig S1b). Such crude parallel bedding, typically represented as gradual
760 alternations of fine and coarser pumice lapilli at a dm-scale, reflects temporal variations in
761 eruptive intensity and is commonly found in the pyroclastic fall deposits of most MER
762 volcanoes and other peralkaline rhyolite volcanoes such as Pantelleria (Orsi et al. 1991) or
763 Monte Pilato (Lipari; Davì et al. 2011) in Italy. These variations may reflect a typical pulsating
764 style of activity controlled by the degassing dynamics in these moderately low-viscosity,
765 crystal-poor magmas (Di Carlo et al. 2010; Di Genova et al. 2013; Neave et al. 2012);
766 however the eruption dynamics, including initiation, evolution and duration of events, and
767 resulting tephra dispersal patterns of pumice cone forming eruptions remain poorly
768 understood.

769

770 ***4d. Chronology and preservation***

771 In the latest Pleistocene and Holocene timeframe, the scarcity of useful material for
772 radiocarbon dating (e.g. charcoal embedded in pyroclastic deposits) from terrestrial sections
773 in the MER provides a great challenge to constrain absolute chronologies and eruptive rates
774 of silicic *vs.* mafic volcanism. In the absence of absolute chronologies, subtle variations in
775 glass major element chemical composition between otherwise similar deposits allow us to
776 fingerprint units and constrain relative stratigraphies and minimum amounts of eruptive
777 events in the recent geological past. At some volcanoes however, additional chemical data

778 such as glass trace element or mineral major element composition (e.g. Albert et al. 2012;
779 Rawson et al. 2015) might allow us to refine correlations in addition to stratigraphic
780 constraints.

781 The most detailed records of Late Quaternary eruptions are from settings where
782 pyroclastic deposits are interbedded with lacustrine deposits containing macrofossil remains
783 (Corbetti, Aluto). At Aluto, the Late Quaternary pyroclastic – lacustrine sequences exposed
784 on land as a result of extensive lake level fluctuations (Benvenuti et al. 2002, 2013; Le Turdu
785 et al. 1999) provide scope to integrate these sequences with lake sediment cores (Chalié
786 and Gasse 2002) into a robust chronological framework that allows the study of temporal
787 variations in and interactions between volcanism, tectonic activity and the
788 palaeoenvironment.

789 Deposition of pyroclastic deposits in lakes may favour their preservation in the geological
790 record, as the terrestrial environment is more prone to weathering and erosion; and it is
791 well known that lacustrine sequences tend to preserve more complete records of volcanism
792 than terrestrial sequences alone (e.g. Bertrand et al. 2014; Fontijn et al. 2016; Green et al.
793 2016). The lack of exposed lacustrine sequences North of Aluto does therefore potentially
794 bias the preserved record to the largest of events. Note, however, that apart from near
795 Aluto, most of our studied sections at all the other volcanoes are in fact terrestrial. It is
796 possible that the relatively small-scale (e.g. VEI 3 and below) events are missing from these
797 sequences, but we would expect abundant evidence for VEI 4 and above events to be
798 preserved in soil sequences had they occurred in the recent geological past (e.g. Brown et
799 al. 2014; Fontijn et al. 2010; Pyle 2016).

800 The new geochemical data and observations of proximal pyroclastic deposits from all the
801 major silicic MER volcanic complexes presented in this paper will allow improved
802 tephrochronological correlations between Late Quaternary sedimentary archives across
803 central Ethiopia (e.g. Martin-Jones et al. 2017; Tiercelin et al. 2008). Such regional-scale
804 correlations of proximal with more distal records will in return allow the fine-tuning of our
805 eruptive chronologies and frequencies, as well as constrain eruption magnitudes and
806 dispersal patterns important for future hazard assessment. Studies limited to tephras in
807 lacustrine settings (e.g. Martin-Jones et al. 2017) may provide constraints on frequencies of
808 events, but cannot highlight the complexity and diversity of eruptive styles and eruption
809 dynamics. At best such studies are complementary to field-based volcanology to understand
810 volcanic hazards. It is critical that this complexity is well-documented, including from
811 detailed field observations of proximal deposits, before undertaking hazard assessments
812 that ultimately feed into risk management policies.

813

814 **5. Conclusions**

815 Geological evidence and current geophysical unrest at many (Biggs et al. 2011; Hutchison et
816 al. 2016a) on-axis silicic MER volcanoes suggests that they remain active and are likely to
817 erupt again in the future. Here we present new fieldwork and geochemical data of late
818 Quaternary silicic tephra deposits in the MER. Our work suggests that potential volcanic
819 hazards and risks at the central MER silicic caldera systems vary widely between each
820 complex, despite similarities in their structure, chemical composition and long-term
821 evolution. Corbetti and Aluto have both been highly active in the Late Quaternary. Their
822 eruption frequencies of 1-3 events per millennium place them amongst the most frequently

active volcanoes for moderate-scale explosive eruptions in East Africa. Some recent MER eruptions were of sub-Plinian scale, depositing tens of centimetres of pumice and ash at present-day densely populated rural areas as well as urbanised population centres. In addition to evidence of explosive activity, most silicic MER complexes have also experienced recent silicic effusive activity in the form of thick obsidian lava flows. The striking variety of eruptive style and rates at the seemingly similar volcanoes along the MER requires a detailed evaluation of volcanic hazard and risk at a regional scale in this (and other) part(s) of the East African Rift System to incorporate reconnaissance studies on each individual centre, and questions the use of analogies to inform hazard and risk mitigation policies.

Acknowledgements

This work was funded by the Natural Environment Research Council grant NE/L013932/1 (RiftVolc) and a Boise Fund grant from the Department of Zoology, University of Oxford. Fieldwork and sample export was kindly permitted by national and local authorities of the Oromia and Southern Nations, Nationalities and Peoples Regions. We are very grateful for the professional logistical support provided by Ethioder and their drivers, and field assistance by Ben Clarke, Eliza Calder, Tim Greenfield,Yelebe Birhanu and Samantha Engwell. Céline Vidal and Yves Moussallam are kindly acknowledged for helpful observations near the Shala caldera. Hazel Farndale assisted with preparation of Aluto samples. Selected samples from the Hawassa and Tilo lake cores were kindly provided by Angela Lamb. Background maps for figures are Shuttle Radar Topography Mission Digital Elevation Model data at 1 arcsecond resolution and were retrieved from the NASA Land Processes Distributed Active Archive Center Products (http://earthexplorer.usgs.gov); additional data

such as settlements and lakes, and topography were retrieved from http://naturalearthdata.com. Editorial handling by Kelly Russell and reviews by Karoly Nemeth and an anonymous reviewer were greatly appreciated.

References

Abdulkadir, Y.A., Eritro, T.H., 2017. 2D resistivity imaging and magnetic survey for characterization of thermal springs: A case study of Gergedi thermal springs in the northwest of Wonji, Main Ethiopian Rift, Ethiopia. Journal of African Earth Sciences, 133: 95-103.

Admassu Bahiru, E., 2007. Structural study and its effect on thermal activities of Tulu Moye – Gedemsa Area. Master of Science Thesis, Addis Ababa University, Department of Earth Sciences, 88pp.

Abebe, B., Acocella, V., Korme, T. & Ayalew, D., 2007. Quaternary faulting and volcanism in the Main Ethiopian Rift. Journal of African Earth Sciences, 48: 115 - 124.

Abebe, T., Manetti, P., Bonini, M., Corti, G., Innocenti, F., Mazzarini, F. and Pecksay, Z., 2005. Geological map (scale 1:200,000) of the northern Main Ethiopian Rift and its implications for the volcano-tectonic evolution of the rift. Geological Society of America Map and Chart Series, MCH094.

Acocella, V., Korme, T., Salvini, F. and Funiciello, R., 2002. Elliptic calderas in the Ethiopian Rift: control of pre-existing structures. Journal of Volcanology and Geothermal Research, 119(1–4): 189-203.

Albert, P.G., Tomlinson, E.L., Smith, V.C., Di Roberto, A., Todman, A., Rosi, M., Marani, M., Muller, W. and Menzies, M.A., 2012. Marine-continental tephra correlations: Volcanic glass geochemistry from the Marsili Basin and the Aeolian Islands, Southern Tyrrhenian Sea, Italy. Journal of Volcanology and Geothermal Research, 229–230: 74-94.

Aspinall, W., Auker, M., Hincks, T., Mahony, S., Nadim, F., Pooley, J., Sparks, S. and Syre, E.,

2011. Volcano Hazard and Exposure in GFDRR Priority Countries and Risk Mitigation Measures. NGI Report 20100806, World Bank - Global Facility for Disaster Reduction and Recovery, 309pp

Auker, M.R., Sparks, R.S.J., Jenkins, S.F., Aspinall, W., Brown, S.K., Deligne, N.I., Jolly, G., Loughlin, S.C., Marzocchi, W., Newhall, C.G., Palma, J.L., 2015. Development of a new global Volcanic Hazard Index (VHI). In: Loughlin, S.C., Sparks, S., Brown, S.K., Jenkins, S.F., Vye-Brown, C. (eds) *Global Volcanic Hazards and Risk*. Cambridge University Press, pp. 349–358

Ayris, P.M. and Delmelle, P., 2012. The immediate environmental effects of tephra emission. Bulletin of Volcanology, 74(9): 1905-1936.

Azais, R.P., Chambord, P., 1931. Cinq années de recherches archéologiques en Ethiopie. Paris, 142pp.

Barker, P., Williamson, D., Gasse, F. & Gibert, E., 2003. Climatic and volcanic forcing revealed in a 50,000-year diatom record from Lake Massoko, Tanzania. Quaternary Research, 60: 368 - 376.

Basell, L.S., 2008. Middle Stone Age (MSA) site distributions in east Africa and their relationship to Quaternary environmental change, refugia and the evolution of *Homo sapiens*. Quaternary Science Reviews, 27: 2484-2498.

Baumann, A., Förstner, U. and Rohde, R., 1975. Lake Shala: Water chemistry, mineralogy and geochemistry of sediments in an Ethiopian Rift lake. Geologische Rundschau, 64(1): 593-609.

Belousov, A. and Belousova, M., 2001. Eruptive process, effects and deposits of the 1996 and the ancient basaltic phreatomagmatic eruptions in Karymskoye Lake, Kamchatka, Russia. Special Publication of the International Association of Sedimentologists, 30: 35-60.

Benvenuti, M., Bonini, M., Tassi, F., Corti, G., Sani, F., Agostini, A., Manetti, P. and Vaselli, O., 2013. Holocene lacustrine fluctuations and deep CO2 degassing in the northeastern Lake Langano Basin (Main Ethiopian Rift). Journal of African Earth Sciences, 77: 1-10.

Benvenuti, M., Carnicelli, S., Belluomini, G., Dainelli, N., Di Grazia, S., Ferrari, G.A., Iasio, C.,

902 Sagri, M., Ventra, D., Atnafu, B. and Kebede, S., 2002. The Ziway–Shala lake basin
903 (main Ethiopian rift, Ethiopia): a revision of basin evolution with special reference to
904 the Late Quaternary. Journal of African Earth Sciences, 35(2): 247-269.

905 Bertrand, S., Daga, R., Bedert, R. and Fontijn, K., 2014. Deposition of the 2011–2012 Cordón
906 Caulle tephra (Chile, 40°S) in lake sediments: Implications for tephrochronology and
907 volcanology. Journal of Geophysical Research: Earth Surface, 119: 2555-2573.

908 Beutel, E., van Wijk, J., Ebinger, C., Keir, D., Agostini, A., 2010. Formation and stability of
909 magmatic segments in the Main Ethiopian and Afar rifts. Earth and Planetary Science
910 Letters, 293: 225 - 235.Bigazzi, B., Bonadonna, F.P., Di Paola, G.M. and Giuliani, A.,
911 1993. K-Ar and fission track ages of the last volcano tectonic phase in the Ethiopian
912 Rift Valley (Tullu Moye' Area), Geology and mineral resources of Somalia and
913 surrounding region, pp. 311-322.

914 Biggs, J., Anthony, E.Y. and Ebinger, C.J., 2009. Multiple inflation and deflation events at
915 Kenyan volcanoes, East African Rift. Geology, 37(11): 979-982.

916 Biggs, J., Bastow, I.D., Keir, D. and Lewi, E., 2011. Pulses of deformation reveal frequently
917 recurring shallow magmatic activity beneath the Main Ethiopian Rift. Geochemistry,
918 Geophysics, Geosystems, 12(9): Q0AB10.

919 Bizouard, H., Di Paola, G.M., 1978. Mineralogy of the Tullu Moje active volcanic area (Arussi:
920 Ethiopian Rift Valley). In: Neumann, E.R., Ramberg, I.B. (eds) *Petrology and*
921 *Geochemistry of Continental Rifts*, Reidel Publishing Company, Dordrecht, Holland,
922 pp. 87–100.

923 Blegen, N., Tryon, C.A., Faith, J.T., Peppe, D.J., Beverly, E.J., Li, B. and Jacobs, Z., 2015. Distal
924 tephras of the eastern Lake Victoria basin, equatorial East Africa: correlations,
925 chronology and a context for early modern humans. Quaternary Science Reviews,
926 122: 89-111.

927 Bluth, G.J.S., Carn, S.A., 2008. Exceptional sulphur degassing from Nyamuragira volcano,
928 1979-2005. International Journal of Remote Sensing 29:6667–6685.
929 http://dx.doi.org/10.1080/01431160802168434.

930 Boccaletti, M., Bonini, M., Mazzuoli, R., Abebe, B., Piccardi, L. and Tortorici, L., 1998.

931 Quaternary oblique extensional tectonics in the Ethiopian Rift (Horn of Africa).
932 Tectonophysics, 287(1): 97-116.

933 Boccaletti, M., Mazzuoli, R., Bonini, M., Trua, T. and Abebe, B., 1999. Plio-Quaternary
934 volcanotectonic activity in the northern sector of the Main Ethiopian Rift:
935 relationships with oblique rifting. Journal of African Earth Sciences, 29(4): 679-698.

936 Bonini, M., Corti, G., Innocenti, F., Manetti, P., Mazzarini, F., Abebe, T. and Pecskay, Z., 2005.
937 Evolution of the Main Ethiopian Rift in the frame of Afar and Kenya rifts propagation.
938 Tectonics, 24(1).

939 Bronk Ramsey, C., 2009. Bayesian analysis of radiocarbon dates. Radiocarbon, 51(1): 337 -
940 360.

941 Brotzu, P., Morbidelli, L., Piccirillo, E.M. and Traversa, G., 1974. Petrological features of
942 boseti mountains, a complex volcanic system in the axial portion of the main
943 Ethiopian rift. Bull Volcanol, 38(1): 206-234.

944 Brown, S., Crosweller, H., Sparks, R., Cottrell, E., Deligne, N., Guerrero, N., Hobbs, L.,
945 Kiyosugi, K., Loughlin, S., Siebert, L. and Takarada, S., 2014. Characterisation of the
946 Quaternary eruption record: analysis of the Large Magnitude Explosive Volcanic
947 Eruptions (LaMEVE) database. Journal of Applied Volcanology, 3(5): 22.

948 Buck, W.R., 2006. The role of magma in the development of the Afro-Arabian Rift System.
949 Geological Society, London, Special Publications, 259(1): 43-54.

950 Buxton, D.R., 1949. Travels in Ethiopia. Drummond, London, 200pp

951 Casey, M. Ebinger, C., Keir, D., Glouaguen, R., Mohamed, F., 2006. Strain accommodation in
952 transitional rifts: extension by magma intrusion and faulting in Ethiopian rift
953 magmatic segments. In: Yirgu, G., Ebinger, C.J., Maguire, P.K.H. (eds) *The Afar*
954 *Volcanic Province within the East African Rift System.* Geological Society of London
955 Special Publications 259:143–164.

956 Chalié, F. and Gasse, F., 2002. Late Glacial–Holocene diatom record of water chemistry and
957 lake level change from the tropical East African Rift Lake Abiyata (Ethiopia).
958 Palaeogeography, Palaeoclimatology, Palaeoecology, 187(3–4): 259-283.

959 Chernet, T., Hart, W.K., Aronson, J.L. and Walter, R.C., 1998. New age constraints on the

960 timing of volcanism and tectonism in the northern Main Ethiopian Rift–southern Afar
961 transition zone (Ethiopia). Journal of Volcanology and Geothermal Research, 80(3–4):
962 267-280.

963 Cole, J.W., 1969. Gariboldi volcanic complex, Ethiopia. Bull Volcanol, 33(2): 566-578.

964 Corti, G., 2008. Control of rift obliquity on the evolution and segmentation of the main
965 Ethiopian rift. Nature Geosci, 1(4): 258-262.

966 Corti, G., 2009. Continental rift evolution: From rift initiation to incipient break-up in the
967 Main Ethiopian Rift, East Africa. Earth Science Reviews, 96: 1-53.

968 Davì, M., De Rosa, R., Donato, P. and Sulpizio, R., 2011. The Lami pyroclastic succession
969 (Lipari, Aeolian Islands): A clue for unravelling the eruptive dynamics of the Monte
970 Pilato rhyolitic pumice cone. Journal of Volcanology and Geothermal Research,
971 201(1–4): 285-300.

972 Dellino, P. and Volpe, L.L., 1995. Fragmentation versus transportation mechanisms in the
973 pyroclastic sequence of Monte Pilato-Rocche Rosse (Lipari, Italy). Journal of
974 Volcanology and Geothermal Research, 64(3–4): 211-231.

975 Di Carlo, I., Rotolo, S.G., Scaillet, B., Buccheri, V. and Pichavant, M., 2010. Phase Equilibrium
976 Constraints on Pre-eruptive Conditions of Recent Felsic Explosive Volcanism at
977 Pantelleria Island, Italy. Journal of Petrology, 51(11): 2245-2276.

978 Di Genova, D., Romano, C., Hess, K.U., Vona, A., Poe, B.T., Giordano, D., Dingwell, D.B. and
979 Behrens, H., 2013. The rheology of peralkaline rhyolites from Pantelleria Island.
980 Journal of Volcanology and Geothermal Research, 249: 201-216.

981 Di Paola, G.M., 1971. Geology of the Corbetti Caldera area (Main Ethiopian Rift Valley). Bull
982 Volcanol, 35(2): 497-506.

983 Di Paola, G.M., 1972. The Ethiopian Rift Valley (between 7° 00′ and 8° 40′ lat. north). Bull
984 Volcanol, 36(4): 517-560.

985 Donovan, A. and Oppenheimer, C., 2018. Imagining the Unimaginable: Communicating
986 Extreme Volcanic Risk. In: Bird, D., Jolly, G., Haynes, K., McGuire, B., Fearnley, C.
987 (eds) Volcanic Crisis Communication: Observing the Volcano World. Springer IAVCEI
988 series Advances in Volcanology, Berlin, Heidelberg, doi 10.1007/11157_2015_16.

989 Ebinger, C., 2005. Continental break-up: The East African perspective. Astronomy &
990 Geophysics, 46: 2.16 - 12.21.

991 Ebinger, C.J. and Casey, M., 2001. Continental breakup in magmatic provinces: An Ethiopian
992 example. Geology, 29(6): 527-530.

993 Emilia, D.A., Last, B.J., Wood, C.A. and Dakin, F.M., 1977. Geophysics and geology of an
994 explosion crater in the Ethiopian rift valley. Bull Volcanol, 40(3): 133-140.Ferguson,
995 D.J., Barnie, T.D., Pyle, D.M., Oppenheimer, C., Yirgu, G., Lewi, E., Kidane, T., Carn, S.
996 and Hamling, I., 2010. Recent rift-related volcanism in Afar, Ethiopia. Earth and
997 Planetary Science Letters 292: 409-418

998

999 Fontijn, K., Ernst, G.G.J., Elburg, M.A., Williamson, D., Abdallah, E., Kwelwa, S., Mbede, E.,
1000 Jacobs, P., 2010. Holocene explosive eruptions in the Rungwe Volcanic Province,
1001 Tanzania. Journal of Volcanology and Geothermal Research, 196: 91 - 110.

1002 Fontijn, K., Rawson, H., Van Daele, M., Moernaut, J., Abarzúa, A.M., Heirman, K., Bertrand,
1003 S., Pyle, D.M., Mather, T.A., De Batist, M., Naranjo, J.-A. and Moreno, H., 2016.
1004 Synchronisation of sedimentary records using tephra: A postglacial
1005 tephrochronological model for the Chilean Lake District. Quaternary Science
1006 Reviews, 137: 234-254.

1007 Fontijn, K., Williamson, D., Mbede, E. and Ernst, G.G.J., 2012. The Rungwe Volcanic Province,
1008 Tanzania – A volcanological review. Journal of African Earth Sciences, 63(0): 12-31.

1009 Gasse, F., 2000. Hydrological changes in the African tropics since the Last Glacial Maximum.
1010 Quaternary Science Reviews, 19: 189-211.

1011 Gasse, F. and Street, F.A., 1978. Late Quaternary Lake-level fluctuations and environments
1012 of the northern Rift valley and Afar region (Ethiopia and Djibouti). Palaeogeography,
1013 Palaeoclimatology, Palaeoecology, 24(4): 279-325.

1014 Gibert, E., Travi, Y., Massault, M., Chernet, T., Barbecot, F. and Laggoun, D.F., 1999.
1015 Comparing carbonate and organic AMS- (super 14) C ages in Lake Abiyata sediments
1016 (Ethiopia); hydrochemistry and paleoenvironmental implications. Radiocarbon,
1017 41(3): 271-286.

1018 Gibert, E., Travi, Y., Massault, M., Tiercelin, J.-J. and Chernet, T., 2002. AMC-14C chronology
1019 of a lacustrine sequence from Lake Langano (Main Ethiopian Rift): Correction and
1020 validation steps in relation with volcanism, lake water and carbon balances.
1021 Radiocarbon, 44(1): 75-92.

1022 Gibson, I.L., 1967. Preliminary account of the volcanic geology of Fantale, Shoa. Bulletin of
1023 the Geophysical Observatory, Addis Ababa, 10: 59-67.

1024 Gibson, I.L., 1970. A pantelleritic welded ash-flow tuff from the Ethiopian Rift Valley. Contr.
1025 Mineral. and Petrol., 28(2): 89-111.

1026 Gibson, I.L., 1974. A review of the geology, petrology and geochemistry of the volcano
1027 Fantale. Bull Volcanol, 38(2): 791-802.

1028 Giordano, F., D'Antonio, M., Civetta, L., Tonarini, S., Orsi, G., Ayalew, D., Yirgu, G., Dell'Erba,
1029 F., Di Vito, M.A. and Isaia, R., 2014. Genesis and evolution of mafic and felsic
1030 magmas at Quaternary volcanoes within the Main Ethiopian Rift: Insights from
1031 Gedemsa and Fanta 'Ale complexes. Lithos, 188(0): 130-144.

1032 Gouin, P., 1979. Earthquake History of Ethiopia and the Horn of Africa. 256.

1033 Green, R.M., Bebbington, M.S., Jones, G., Cronin, S.J. and Turner, M.B., 2016. Estimation of
1034 tephra volumes from sparse and incompletely observed deposit thicknesses. Bulletin
1035 of Volcanology, 78(4): 1-18.

1036 Harris W.C., 1844. The Highlands of Aethiopia (3 Vols, 2nd Edition). Vol III, Longman, Brown,
1037 Green and Longmans, London, 436 pp.

1038 Hunt, J.A., Zafu, A., Mather, T.A., Pyle, D.M. and Barry, P.H., 2017. Spatially variable CO_2
1039 degassing in the Main Ethiopian Rift: Implications for magma storage, volatile
1040 transport, and rift-related Emissions. Geochemistry, Geophysics, Geosystems,
1041 18(10): 3714-3737.

1042 Hutchison, W., Biggs, J., Mather, T.A., Pyle, D.M., Lewi, E., Yirgu, G., Caliro, S., Chiodini, G.,
1043 Clor, L.E. and Fischer, T.P., 2016. Causes of unrest at silicic calderas in the East
1044 African Rift: New constraints from InSAR and soil-gas chemistry at Aluto volcano,
1045 Ethiopia. Geochemistry, Geophysics, Geosystems, 17: n/a-n/a.

1046 Hutchison, W., Fusillo, R., Pyle, D.M., Mather, T.A., Blundy, J.D., Biggs, J., Yirgu, G., Cohen,

1047 B.E., Brooker, R.A., Barfod, D.N. and Calvert, A.T., 2016. A pulse of mid-Pleistocene
1048 rift volcanism in Ethiopia at the dawn of modern humans. Nature Communications,
1049 7: 13192.

1050 Hutchison, W., Mather, T.A., Pyle, D.M., Biggs, J. and Yirgu, G., 2015. Structural controls on
1051 fluid pathways in an active rift system: A case study of the Aluto volcanic complex.
1052 Geosphere.

1053 Hutchison, W., Pyle, D.M., Mather, T.A., Yirgu, G., Biggs, J., Cohen, B.E., Barfod, D.N. and
1054 Lewi, E., 2016. The eruptive history and magmatic evolution of Aluto volcano: new
1055 insights into silicic peralkaline volcanism in the Ethiopian rift. Journal of Volcanology
1056 and Geothermal Research, 328: 9-33.

1057 Jeffery, A.J., Gertisser, R., O'Driscoll, B., Pacheco, J.M., Whitley, S., Pimentel, A. and Self, S.,
1058 2016. Temporal evolution of a post-caldera, mildly peralkaline magmatic system:
1059 Furnas volcano, São Miguel, Azores. Contr. Mineral. and Petrol., 171(5): 42.

1060 JICA, 2012. The Study on Groundwater Resources Assessment in the Rift Valley Lakes Basin
1061 in the Federal Democratic Republic of Ethiopia. Japan International Cooperation
1062 Agency, Kokusai Kogyo Co. Ltd. and Ministry of Water and Energy (MoWE), The
1063 Federal Democratic Republic of Ethiopia. Final Report (Supporting Report and Data
1064 Book), 95pp and 25 pp.

1065 Jochum, K.P., Stoll, B., Herwig, K., Willbold, M., Hofmann, A.W., Amini, M., Aarburg, S.,
1066 Abouchami, W., Hellebrand, E., Mocek, B., Raczek, I., Stracke, A., Alard, O., Bouman,
1067 C., Becker, S., Dücking, M., Brätz, H., Klemd, R., de Bruin, D., Canil, D., Cornell, D., de
1068 Hoog, C.-J., Dalpé, C., Danyushevsky, L., Eisenhauer, A., Gao, Y., Snow, J.E.,
1069 Groschopf, N., Günther, D., Latkoczy, C., Guillong, M., Hauri, E.H., Höfer, H.E.,
1070 Lahaye, Y., Horz, K., Jacob, D.E., Kasemann, S.A., Kent, A.J.R., Ludwig, T., Zack, T.,
1071 Mason, P.R.D., Meixner, A., Rosner, M., Misawa, K., Nash, B.P., Pfänder, J., Premo,
1072 W.R., Sun, W.D., Tiepolo, M., Vannucci, R., Vennemann, T., Wayne, D. and
1073 Woodhead, J.D., 2006. MPI-DING reference glasses for in situ microanalysis: New
1074 reference values for element concentrations and isotope ratios. Geochem. Geophys.
1075 Geosyst., 7(2): Q02008.

1076 Jochum, K.P., Weis, U., Stoll, B., Kuzmin, D., Yang, Q., Raczek, I., Jacob, D.E., Stracke, A.,

1077 Birbaum, K., Frick, D.A., Günther, D. and Enzweiler, J., 2011. Determination of
1078 Reference Values for NIST SRM 610–617 Glasses Following ISO Guidelines.
1079 Geostandards and Geoanalytical Research, 35(4): 397-429.

1080 Keir, D., Bastow, I.D., Corti, G., Mazzarini, F. and Rooney, T.O., 2015. The origin of along-rift
1081 variations in faulting and magmatism in the Ethiopian Rift. Tectonics, 34(3): 464-477.

1082 Keir, D., Stuart, G.W., Jackson, A. and Ayele, A., 2006. Local Earthquake Magnitude Scale and
1083 Seismicity Rate for the Ethiopian Rift. Bulletin of the Seismological Society of
1084 America, 96(6): 2221-2230.

1085 Kendall, J.-M., Stuart, G.W., Ebinger, C.J., Bastow, I.D., Keir, D., 2005. Magma-assisted rifting
1086 in Ethiopia. Nature, 433: 146 - 148.

1087 Keranen, K., Klemperer, S.L., Gloaguen, R. and Group, E.W., 2004. Three-dimensional seismic
1088 imaging of a protoridge axis in the Main Ethiopian rift. Geology, 32(11): 949-952.

1089 Keynes, S., 2007 (ed). Ethiopian encounters: Sir William Cornwallis Harris and the British
1090 Mission to the Kingdom of Shewa (1841-3). Fitzwilliam Museum, Cambridge, 72 pp.

1091 Le Bas, M.J., LeMaitre, R.W., Streckheisen, A., Zanettin, B., 1986. Chemical classification of
1092 volcanic rocks based on the total alkali–silica diagram. Journal of Petrology 27, 745–
1093 750.

1094 Le Turdu, C., Tiercelin, J.-J., Gibert, E., Travi, Y., Lezzar, K.-E., Richert, J.-P., Massault, M.,
1095 Gasse, F., Bonnefille, R., Decobert, M., Gensous, B., Jeudy, V., Tamrat, E.,
1096 Mohammed, M.U., Martens, K., Atnafu, B., Chernet, T., Williamson, D. and Taieb, M.,
1097 1999. The Ziway–Shala lake basin system, Main Ethiopian Rift: Influence of
1098 volcanism, tectonics, and climatic forcing on basin formation and sedimentation.
1099 Palaeogeography, Palaeoclimatology, Palaeoecology, 150(3–4): 135-177.

1100 Leat, P.T., 1984. Geological evolution of the trachytic caldera volcano Menengai, Kenya Rift
1101 Valley. Journal of The Geological Society of London, 141: 1057-1069.

1102 Lézine, A.-M., Ivory, S.J., Braconnot, P. and Marti, O., 2017. Timing of the southward retreat
1103 of the ITCZ at the end of the Holocene Humid Period in Southern Arabia: Data-model
1104 comparison. Quaternary Science Reviews, 164: 68-76.

1105 MacDonald, R., 1974. Nomenclature and petrochemistry of the peralkaline oversaturated

extrusive rocks. Bulletin Volcanologique, 38(2): 498-516.

Macdonald, R., Bagiński, B., Ronga, F., Dzierżanowski, P., Lustrino, M., Marzoli, A. and Melluso, L., 2012. Evidence for extreme fractionation of peralkaline silicic magmas, the Boseti volcanic complex, Main Ethiopian Rift. Miner Petrol, 104(3): 163-175.

Mahood, G.A., 1984. Calderas associated with strongly peralkaline volcanic rocks. Journal of Geophysical Research 89:8540–8552.

Mahood, G.A. and Hildreth, W., 1986. Geology of the peralkaline volcano at Pantelleria, Strait of Sicily. Bulletin of Volcanology, 48(2): 143-172.

Manville, V., Segschneider, B., Newton, E., White, J.D.L., Houghton, B.F. and Wilson, C.J.N., 2009. Environmental impact of the 1.8 ka Taupo eruption, New Zealand: Landscape responses to a large-scale explosive rhyolite eruption. Sedimentary Geology, 220(3): 318-336.Martin-Jones, C.M., Lane, C.S., Pearce, N.J., Smith, V.C., Lamb, H.F., Schaebitz, F., Viehberg, F., Brown, M.C., Frank, U. and Asrat, A., 2017. Recurrent explosive eruptions from a high-risk Main Ethiopian Rift volcano throughout the Holocene. Geology, 45(12): 1127-1130.

Mengistu Darge, Y., Tesfaw Hailu, B., Atnafu Muluneh, A., Kidane, T., 2017. Detection of geothermal anomalies using Landsat 8 TIRS data in Tulu Moye geothermal prospect, Main Ethiopian Rift. The 4th National GIS Summit, 13-15 January 2017, Bahir Dar University, Ethiopia.

Meyer, W., Pilger, A., Rosler, A., Stets, J., 1975. Tectonic evolution of the northern part of the Main Ethiopian Rift in Southern Ethiopia. In: Pilger, A., Rosler, A. (eds) *Afar Depression of Ethiopia*. Schweizerbart, Stuttgart, pp. 352–362.

Mohr, P., 1962. The Ethiopian Rift System. Bulletin of the Geophysical Observatory, Addis Ababa, 3(1): 33-62.

Mohr, P., Mitchell, J.G. and Raynolds, R.G.H., 1980. Quaternary volcanism and faulting at O'A caldera, central ethiopian rift. Bull Volcanol, 43(1): 173-189.

Mohr, P.A., 1966. Chabbi volcano (ethiopia). Bull Volcanol, 29(1): 797-815.

Mohr, P.A. and Wood, C.A., 1976. Volcano spacings and lithospheric attenuation in the Eastern Rift of Africa. Earth and Planetary Science Letters, 33(1): 126-144.

1135 Morton, W.H., Rex, D.C., Mitchell, J.G. and Mohr, P., 1979. Riftward younging of volcanic
1136 units in the Addis Ababa region, Ethiopian rift valley. Nature, 280(5720): 284-288.

1137 Neave, D.A., Fabbro, G., Herd, R.A., Petrone, C.M. and Edmonds, M., 2012. Melting,
1138 Differentiation and Degassing at the Pantelleria Volcano, Italy. Journal of Petrology,
1139 53(3): 637-663.

1140 Negash, A., Alene, M., Brown, F.H., Nash, B.P. and Shackley, M.S., 2007. Geochemical
1141 sources for the terminal Pleistocene/early Holocene obsidian artifacts of the site of
1142 Beseka, central Ethiopia. Journal of Archaeological Science, 34(8): 1205-1210.

1143 Newhall, C.G., Dzurisin, D., 1988. Historical unrest at large calderas of the world, 1108 pp.

1144 Newhall, C.G., Self, S., 1982. The Volcanic Explosivity Index (VEI) - An estimate of explosive
1145 magnitude for historical volcanism. Journal of Geophysical Research, 87(C2): 1231-
1146 1238.

1147 Orsi, G., Ruvo, L. and Scarpati, C., 1991. The recent explosive volcanism at Pantelleria.
1148 Geologische Rundschau, 80(1): 187-200.

1149 Pearce, N.J.G., Abbott, P.M. and Martin-Jones, C., 2014. Microbeam methods for the
1150 analysis of glass in fine-grained tephra deposits: a SMART perspective on current and
1151 future trends. Geological Society, London, Special Publications, 398(1): 29-46.

1152 Peccerillo, A., Barberio, M.R., Yirgu, G., Ayalew, D., Barbieri, M. and Wu, T.W., 2003.
1153 Relationships between Mafic and Peralkaline Silicic Magmatism in Continental Rift
1154 Settings: a Petrological, Geochemical and Isotopic Study of the Gedemsa Volcano,
1155 Central Ethiopian Rift. Journal of Petrology, 44(11): 2003-2032.

1156 Poppe, S., Smets, B., Fontijn, K., Rukeza, M.B., De Marie Fikiri Migabo, A., Milungu, A.K.,
1157 Namogo, D.B., Kervyn, F. and Kervyn, M., 2016. Holocene phreatomagmatic
1158 eruptions alongside the densely populated northern shoreline of Lake Kivu, East
1159 African Rift: timing and hazard implications. Bulletin of Volcanology, 78(11): 82.

1160 Pyle, D.M., 1989. The thickness, volume and grainsize of tephra fall deposits. Bulletin of
1161 Volcanology, 51(1): 1-15.

1162 Pyle, D.M., 1999. Widely dispersed Quaternary tephra in Africa. Global and Planetary
1163 Change, 21(1–3): 95-112.

Pyle, D.M., 2015. Sizes of Volcanic Eruptions. Encyclopedia of Volcanoes, 2: 257-264.

Pyle, D.M., 2016. Field observations of tephra fallout deposits. In: Mackie, S., Cashman, K., Ricketts, H., Rust, A., Watson, M. (eds) *Volcanic Ash. Hazard Observation*. Elsevier, p25–38.

Rampey, M.L., Oppenheimer, C., Pyle, D.M. and Yirgu, G., 2010. Caldera-forming eruptions of the Quaternary Kone Volcanic Complex, Ethiopia. Journal of African Earth Sciences, 58(1): 51-66.

Rapprich, V., Čížek, D., Daniel, K., Firdawok, L., Habtamu, B., Hroch, T., Kopačková, V.,Málek, J., Malík, J., Mišurec, J., Orgoň, A., Šebesta, J., Šíma, J., Tsigehana, T., Verner, K., Yewubinesh, B., 2013. Explanation Booklet to the Set of Geosciencemaps of Ethiopia at scale 1:50,000, subsheet 0738-C4 Hawasa. Czech Geological Survey / Aquatest / Geological Survey of Ethiopia, Praha / Addis Ababa, Czech Republic / Ethiopia, pp. 1–46

Rapprich, V., Žáček, V., Verner, K., Erban, V., Goslar, T., Bekele, Y., Legesa, F., Hroch, T. and Hejtmánková, P., 2016. Wendo Koshe Pumice: The latest Holocene silicic explosive eruption product of the Corbetti Volcanic System (Southern Ethiopia). Journal of Volcanology and Geothermal Research, 310: 159-171.

Rawson, H., Naranjo, J.A., Smith, V.C., Fontijn, K., Pyle, D.M., Mather, T.A. and Moreno, H., 2015. The frequency and magnitude of post-glacial explosive eruptions at Volcán Mocho-Choshuenco, southern Chile. Journal of Volcanology and Geothermal Research, 299(0): 103-129.

Reimer, P.J., Bard, E., Bayliss, A., Beck, J.W., Blackwell, P.G., Bronk Ramsey, C., Buck, C.E., Cheng, H., Edwards, R.L., Friedrich, M., Grootes, P.M., Guilderson, T.P., Haflidason, H., Hajdas, I., Hatté, C., Heaton, T.J., Hoffmann, D.L., Hogg, A.G., Hughen, K.A., Kaiser, K.F., Kromer, B., Manning, S.W., Niu, M., Reimer, R.W., Richards, D.A., Scott, E.M., Southon, J.R., Staff, R.A., Turney, C.S.M. and van der Plicht, J., 2013. IntCal13 and Marine13 radiocarbon age calibration curves 0-50,000 years cal BP. Radiocarbon, 55(4): 1869-1887.

Robertson, E., Biggs, J., Edmonds, M., Clor, L., Fischer, T.P., Vye-Brown, C., Kianji, G., Koros, W. and Kandie, R., Diffuse degassing at Longonot volcano, Kenya: Implications for

1194 CO2 flux in continental rifts. Journal of Volcanology and Geothermal Research.

1195 Ronga, F., Lustrino, M., Marzoli, A. and Melluso, L., 2010. Petrogenesis of a basalt-
1196 comendite-pantellerite rock suite: the Boseti Volcanic Complex (Main Ethiopian Rift).
1197 Miner Petrol, 98(1-4): 227-243.

1198 Rooney, T., Furman, T., Bastow, I., Ayalew, D. and Yirgu, G., 2007. Lithospheric modification
1199 during crustal extension in the Main Ethiopian Rift. Journal of Geophysical Research:
1200 Solid Earth, 112(B10): n/a-n/a.

1201 Rooney, T.O., Bastow, I.D., Keir, D., 2011. Insights into extensional processes during magma
1202 assisted rifting: Evidence from aligned scoria cones. Journal of Volcanology and
1203 Geothermal Research, 201: 83-96.

1204 Rooney, T.O., Furman, T., Yirgu, G. and Ayalew, D., 2005. Structure of the Ethiopian
1205 lithosphere: Xenolith evidence in the Main Ethiopian Rift. Geochimica et
1206 Cosmochimica Acta, 69(15): 3889-3910.

1207 Scott, S.C., 1980. The Geology of Longonot Volcano, Central Kenya: A Question of Volumes.
1208 Philosophical Transactions of the Royal Society of London: Mathematical and
1209 Physical Sciences, 296(1420): 437-465.

1210 Siebert, L., Simkin, T. and Kimberly, P., 2010. Volcanoes of the World - Third Edition.
1211 University of California Press, Berkeley, 568 pp.

1212 Siegburg, M., Gernon, T.M., Bull, J.M., Keir, D., Barfod, D.N., Taylor, R.N., Abebe, B., Ayele,
1213 A., 2018. Geological evolution of the Boset-Bericha Volcanic Complex, Main
1214 Ethiopian Rift: $^{40}Ar/^{39}Ar$ evidence for episodic Pleistocene to Holocene volcanism.
1215 Journal of Volcanology and Geothermal Research,
1216 https://doi.org/10.1016/j.jvolgeores.2017.12.014

1217 Thrall, R., 1973. Gadamsa Caldera, Ethiopia. Centre for Astrophysics, Dartmouth College,
1218 Reprint Series, 280: 71-80.

1219 Tiercelin, J.J., Gibert, E., Umer, M., Bonnefille, R., Disnar, J.R., Lézine, A.M., Hureau-
1220 Mazaudier, D., Travi, Y., Keravis, D. and Lamb, H.F., 2008. High-resolution
1221 sedimentary record of the last deglaciation from a high-altitude lake in Ethiopia.
1222 Quaternary Science Reviews, 27(5–6): 449-467.

1223 Trua, T., Deniel, C. and Mazzuoli, R., 1999. Crustal control in the genesis of Plio-Quaternary
1224 bimodal magmatism of the Main Ethiopian Rift (MER): geochemical and isotopic (Sr,
1225 Nd, Pb) evidence. Chemical Geology, 155(3–4): 201-231.

1226 USAID (2017) Power Africa Programme; http://www.usaid.gov/powerafrica; accessed June
1227 2017.

1228 Vogel, N., Nomade, S., Negash, A. and Renne, P.R., 2006. Forensic 40Ar/39Ar dating: a
1229 provenance study of Middle Stone Age obsidian artifacts from Ethiopia. Journal of
1230 Archaeological Science, 33(12): 1749-1765.

1231 Wadge, G., Biggs, J., Lloyd, R. and Kendall, J.-M., 2016. Historical Volcanism and the State of
1232 Stress in the East African Rift System. Frontiers in Earth Science, 4(86).

1233 Wauthier, C., Cayol, V., Poland, M., Kervyn, F., d'Oreye, N., Hooper, A., Samsonov, S.,
1234 Tiampo, K. and Smets, B., 2013. Nyamulagira's magma plumbing system inferred
1235 from 15 years of InSAR. Geological Society, London, Special Publications, 380(1): 39-
1236 65.

1237 White, J.D.L. and Valentine, G.A., 2016. Magmatic versus phreatomagmatic fragmentation:
1238 Absence of evidence is not evidence of absence. Geosphere, 12(5).

1239 Wilks, M., Kendall, J.M., Nowacki, A., Biggs, J., Wookey, J., Birhanu, Y., Ayele, A. and Bedada,
1240 T., 2017. Seismicity associated with magmatism, faulting and hydrothermal
1241 circulation at Aluto Volcano, Main Ethiopian Rift. Journal of Volcanology and
1242 Geothermal Research 340: 52-67

1243 Williams, F.M., Williams, M.A.J. and Aumento, F., 2004. Tensional fissures and crustal
1244 extension rates in the northern part of the Main Ethiopian Rift. Journal of African
1245 Earth Sciences, 38(2): 183-197.

1246 Wilson, T., Stewart, C., Sword-Daniels, V., Leonard, G., Johnston, D., Cole, J., Wardman, J.,
1247 Wilson, G., Barnard, S., 2012. Volcanic ash impacts on critical infrastructure. Physics
1248 and Chemistry of the Earth, 45-45: 5-23.

1249 WoldeGabriel, G., Aronson, J.L. and Walter, R.C., 1990. Geology, geochronology, and rift
1250 basin development in the central sector of the Main Ethiopia Rift. Geological Society
1251 of America Bulletin, 102(4): 439-458.

Wolfenden, E., Ebinger, C., Yirgu, G., Deino, A., Ayalew, D., 2004. Evolution of the northern Main Ethiopian Rift: Birth of a Triple Junction. Earth and Planetary Science Letters, 224: 213 - 228.

Figures

Fig 1 Overview of Main Ethiopian Rift with Late Pleistocene – Holocene active volcanic centres, small eruptive centres and main tectonic features. Outcrops visited (yellow dots) span most of the MER; lake sediment cores with described tephra horizons indicated in blue. For clarity, the Wonji Faults are not drawn; they largely control the spatial distribution of basaltic small eruptive centres along the rift axis.

Fig 2 Isopach map of Wendo Koshe Younger Pumice (WKYP, turquoise) deposit from Corbetti as identified from lateral tracing in the field and geochemical analysis. Thicknesses of individual measurements in cm; contours are drawn tentatively where dispersal is poorly constrained. Thickness values for Bedded Pumice (in orange) are also given in cm but no contours are drawn. Reference sites for stratigraphy (named MER- and 3-digit number) are schematically illustrated in Fig 3. Caldera wall and post-caldera edifices are also outlined (A: Artu, U: Urji, C: Chabbi). Extra-caldera small eruptive centres (SECs) to the east of Lake Hawassa are basaltic and possibly phreatomagmatic in origin (Rapprich et al. 2013). A rhyolitic tuff complex immediately north of the lake is onlapped by Chabbi obsidian flows and may also be phreatomagmatic. Other SECs, in the form of magmatic scoria cones, occur north of Corbetti along fractures extending to the Shala Caldera. Post-caldera Tullu Fike

1276 pumice cone complex indicated north of Shala. Other extra-caldera vents north and south of
1277 the caldera, and presumably of basaltic composition, are also of unknown age.

1278 **Fig 3** Schematic representation of Corbetti's composite Holocene pyroclastic stratigraphy;
1279 locations of reference sites indicated on Fig 2. Inset shows major element analyses of
1280 distinct pyroclastic units revealing systematic pantelleritic composition. Non-correlated
1281 Corbetti units indicated as small grey dots. Names and ages of Lake Tilo (TT-) and Hawassa
1282 (AWT-) tephras after Martin-Jones et al. (2017).

1283 **Fig 4** Field photographs for reference sections of Holocene pyroclastic deposits shown in Fig
1284 2-3 (Corbetti) and Fig 5 (Aluto); same colour coding. **(a)** Coarse pumice lapilli breccia of
1285 WKYP covering finer grained Bedded Pumice; black arrow denotes ca. 10-15 cm palaeosol
1286 between deposits. **(b)** Oldest sequence of Holocene pyroclastic deposits exposed in
1287 terrestrial sections as described in this study; black arrow shows sample location of charcoal
1288 dated 7.75 ± 0.04 ka cal BP (Table 3); people for scale; **(c)** Exposure of lacustrine deposits
1289 interbedded with pyroclastic deposits (typically darker grey horizons) in type section A01
1290 (Fig 5); **(d)** Close-up of pyroclastic deposit inferred to be emplaced under water: bottom half
1291 clast-supported pumice lapilli with some intergranular fine ash, top half pumice lapilli
1292 dispersed in more ash-rich matrix; pencil for scale

1293

1294 **Fig 5** Spatial distribution of sample localities at Aluto, with identification of type locality A01
1295 (stratigraphic column on right); some locally correlated deposits colour-coded as in Fig 6,
1296 with deposit thickness indicated in cm; tephra from other sites (grey dots) did not yield
1297 correlations across multiple localities. Selected named outcrops also represented in Fig 4c-d,
1298 6 and S1c-d ("MER" omitted from the 3-digit labels for clarity, "WH_" omitted from other

1299 labels; full details in Supplementary Table 2). SEC: Small Eruptive Centre – those close and
1300 possibly associated to the Aluto complex are distinguished from the ones in East Ziway; TC:
1301 tuff cone; TAC: trachyandesitic scoria cone. High-resolution LIDAR digital elevation model on
1302 the Aluto edifice after Hutchison et al. (2015).

1303

1304 **Fig 6** The glass major element composition of geologically young Aluto pumice samples.
1305 These span a wide range of mostly pantelleritic compositions. Some units can be correlated
1306 on a local scale, including A9 / Qup. Samples highlighted in colour are are colour-coded as in
1307 Fig 5; grey dots represent analyses of samples that could not be correlated between
1308 multiple localities. Glass chemistry for Corbetti samples (Fig 3) given for comparison, and to
1309 highlight potential correlation of sample 150207 found NE of Lake Langano (Fig 5) to
1310 Corbetti source (Fig 3). The complicated fingerprinting of Corbetti samples however requires
1311 additional verification to validate this correlation.

1312 **Fig 7** Overview map of Bora-Baricha, Tullu Moye and Gedemsa area. Both post-caldera
1313 scoria cones near Gedemsa and Tully Moye, as well as rhyolitic lava flows of Tullu Moye are
1314 controlled by the Wonji Fault Belt. SECs indicated in orange have confirmed basaltic glass
1315 composition (samples MER153A and MER157A in Supplementary Table 3a). Gedemsa
1316 caldera is outlined in dark blue, with extent of its post-caldera constructs in pink. The dotted
1317 pink lines highlight low-relief dome-shaped constructs which are presumably also post-
1318 caldera centres of activity. Dots indicate sample sites, and those at Gedemsa are colour-
1319 coded as in Figure 9. Selected outcrops from Figures 8-9 (omitting "MER-", for clarity;
1320 Supplementary Table 2) are named.

Fig 8 (a) Bora-Baricha representative field photos showing alternation of pyroclastic fall deposits and palaeosols (MER147-1/2) and a stack of multiple-metre-thick pyroclastic fall and dilute PDC deposits alternating with poorly developed soils and ash-rich reworked horizons (MER150). These deposits have not been chemically correlated to other units in the region but were most likely sourced from Bora-Baricha or associated edifices; colour-coded with (b) and (c). **(b)** Bora-Baricha and Tullu Moye key stratigraphic sections, spanning all sides of the complex (Fig 7). Many eruptions have emplaced several meters of pyroclastic fall deposits, and most sections show only limited soil formation between events. **(c)** Glass major element composition of Bora-Baricha and Tullu Moye silicic pyroclastic deposits. Bora-Borecha samples are pantelleritic whereas those of Tullu Moye are comenditic. The top unit of section MER150 has a distinct composition to the rest of the sequence and may form a fractionation trend with Tullu Moye comendites.

Fig 9 (a-c) Gedemsa representative field photos: **(a)** MER084, crudely bedded dark grey pumice lapilli breccia alternating with low-angle cross-bedded fine pumice and ash lapilli deposits, presumably related to caldera-forming events, and chemically correlated to MER077; scraper (encircled in yellow) for scale. **(b)** MER087: poorly sorted pumice lapilli and bomb breccia exposed on rim of Kore crater, the most prominent post-caldera centre; pencil for scale. **(c)** MER081: (presumably) post-caldera pumice lapilli breccia deposit exposed underneath cross-bedded indurated tuff deposits associated to mafic volcanism near the NE rim of the caldera. **(d-e)** Gedemsa glass geochemistry for a selection of samples obtained

1344 from multiple syn-caldera pumice breccia deposits and post-caldera pumice deposits
1345 (colour-coded as in Fig 7). The three most FeO-rich deposits originate from the intra-caldera
1346 coalesced domes Kelo, Dima and Kore. Three more chemically distinct pumice fall deposits
1347 are identified and were sampled from sections immediately NE and E of the caldera. Each of
1348 these presumably represents an individual moderately explosive post-caldera eruption. The
1349 age of these post-caldera events is not known.

1350

1351 **Fig 10** Overview map of Boset volcanic complex, with overlain isopach map (thickness in cm)
1352 of the Boset Pumice deposit. Tephra was mainly dispersed westward, with accumulations
1353 multiple metres thick on the lower western flanks of the complex. The dispersal towards the
1354 north and east is poorly constrained; however none of the outcrops in those regions
1355 revealed the presence of substantial pumice fall deposits. Named outcrops are those listed
1356 in Fig 11. ([1]) One lobe of trachyandesitic lava was dated at 4.2 ± 3.2 ka (Siegburg et al. 2018)
1357 and may correspond to Scoria #2 in our type section MER108 (Fig 11).

1358 **Fig 11** Glass geochemistry and type stratigraphy of the most recent pyroclastic deposits at
1359 Boset volcanic complex; **(a)** Total Alkali – Silica diagram (after Le Bas et al. 1986) showing
1360 rhyolitic pumice deposits and basaltic scoria deposits. A scoria fall deposit interbedded in
1361 the type stratigraphy (unit #2) has a basaltic trachyandesite composition and possibly
1362 corresponds to the eruption of lava flows in the saddle between Gudda and Bericha
1363 (Siegburg et al. 2018). The most evolved rhyolites are from a sequence of altered coarse
1364 grey pumice fall deposits and finely parallel to cross-bedded dilute PDC deposits, which may
1365 relate to a caldera-forming event; **(b)** Classification diagram of peralkaline rhyolites (after
1366 MacDonald 1974) shows the three most recent pumice fall units to have a pantelleritic

composition, whereas the oldest pumice fall (#5) is comenditic. There may be multiple comendite falls but more field and geochemical data are required to verify this. Mafic samples in this plot are given for reference only. **(c)** Schematic log of type stratigraphic section for recent pyroclastic deposits, colour-coded as in **(a)** and **(b)**; **(d)** Field photograph of "Boset Pumice", unit #1, in locality MER113 (Fig 10).

Fig 12 Overview map of Kone caldera complex and Fentale, with indication of basaltic scoria cones which erupted as recently as 1810-1820 AD (Harris 1844; Supplementary Table 1). Fentale has experienced post-caldera silicic volcanism in the form of obsidian lava flows erupted from vents in the caldera floor and on the NE, E, SE and W flanks. At Kone there is no evidence for post-caldera silicic volcanism.

Fig 13 Glass chemical composition of a selection of scoria fall deposits and pumice lapilli breccia associated to caldera-forming events at the Kone caldera complex. Corresponding map units of Rampey et al. (2010) indicated in brackets. Glass composition of obsidian source rocks from Kone after Negash et al. (2007).

Tables

Table 1 Average glass major element composition of main units at each volcanic centre (full dataset in Supplementary Table 3a)

Table 2 Synoptic summary of MER post-caldera silcic and mafic eruptive activity, as constrained by edifice morphology, field observations, geochemistry, geochronology and previously published literature. Items for which no information is available have been left blank. PDC: pyroclastic density current.

1389 **Table 3** New Accelerator Mass Spectroscopy radiocarbon date for charcoal sample buried
1390 under Corbetti pyroclastic fall deposit. Analysis was performed at Beta Analytic Inc., Florida,
1391 USA. Ages are reported as years before present (yr BP), "present" being 1950 CE, as per
1392 international convention. Calibration was performed in Oxcal v4.3 using the IntCal13
1393 calibration curve (http://c14.arch.ox.ac.uk; Bronk Ramsey 2009; Reimer et al. 2013).

1394 **Supplementary Information**

1395 **Supplementary Figure S1** Field photographs for reference sections of Corbetti and Aluto
1396 Holocene pyroclastic deposits. **(a)** Stack of pyroclastic deposits separated by thin soil
1397 horizons representative of intra-caldera Corbetti sequence (including Bedded Pumice); black
1398 arrow denotes fall deposit within sequence of small-scale PDC deposits (Fig 3); people for
1399 scale; **(b)** Typically rhythmically bedded nature of Bedded Pumice in its proximal sections;
1400 trowel for scale; **(c)** Crudely bedded pumice fall deposits found ubiquitously on the edifice –
1401 type locality for "Qup" unit defined by Hutchison et al (2016b); scraper for scale. **(d)** Section
1402 through pumice cone displaying >10 m rhythmically bedded pumice and ash fall deposits;
1403 close-up observations of this sections were not possible due to steep cliff;

1404 **Supplementary Table 1** Overview of central silicic volcanoes in the Main Ethiopian Rift
1405 (MER), with indication of their alternative names present in the literature and most recent
1406 confirmed eruption. Volcano Number after the Smithsonian Institute Global Volcanism
1407 Program Database (http://volcano.si.edu).

1408 **Supplementary Table 2** Main Ethiopian Rift outcrop localities with brief description of
1409 geology. All coordinates in Latitude - Longitude, WGS84 datum. Sample names (as listed in
1410 Supplementary Table 3a) follow outcrop name followed by a letter (e.g. A, B, etc.).

Table S3a. EMP data for all samples analysed in this study. Outcrop coordinates for terrestrial outcrops (names starting with "MER") are listed in Supplementary Table S2. Points refer to individual analysis spots, each on an individual patch of glass, avoiding visible crystals. Analyses suggesting an influence of (hidden) crystals have been omitted. Samples are grouped by volcano (south to north, Fig 1) and units are identified where possible. Only the most widely distributed units are given a unique name. Other units are identified as "NA" followed by the unit number of their corresponding section (in stratigraphic order, #1 being the youngest). Run refers to date analyses were acquired; corresponding secondary standard analyses and analytical conditions for all runs, ordered by date, are listed in Supplementary Table S3b. Analyses are normalised to volatile-free composition. Cl was also omitted from normalisation because it was not analysed for all samples.

Table S3b EMP analyses of secondary glass standards (non-normalised) run together with samples. All analyses were run at 15 kV accelerating voltage, 6 (or 4) nA beam current, and 10 (or 5) µm beam width. Standards were run at the start, regularly during and at the end of each run to monitor data quality. Error bars, also reported with the samples, are calculated as 2 x relative standard deviation on the standard analyses and hence represent precision of the data. Data accuracy is colour-coded on the average for each standard analysis during each run: green values are within 1s of the preferred values, orange within 2s, and red out of the 2s range. Standards used are ATHO-G (rhyolite), NIST-612 (synthetic glass), StHs6/80-G (andesite/dacite) and ML3B-G (basalt), and cover the range of expected values in our sample set. Preferred values, after Jochum et al. (2006, 2011), can also be consulted on GeoREM (http://georem.mpch-mainz.gwdg.de/).

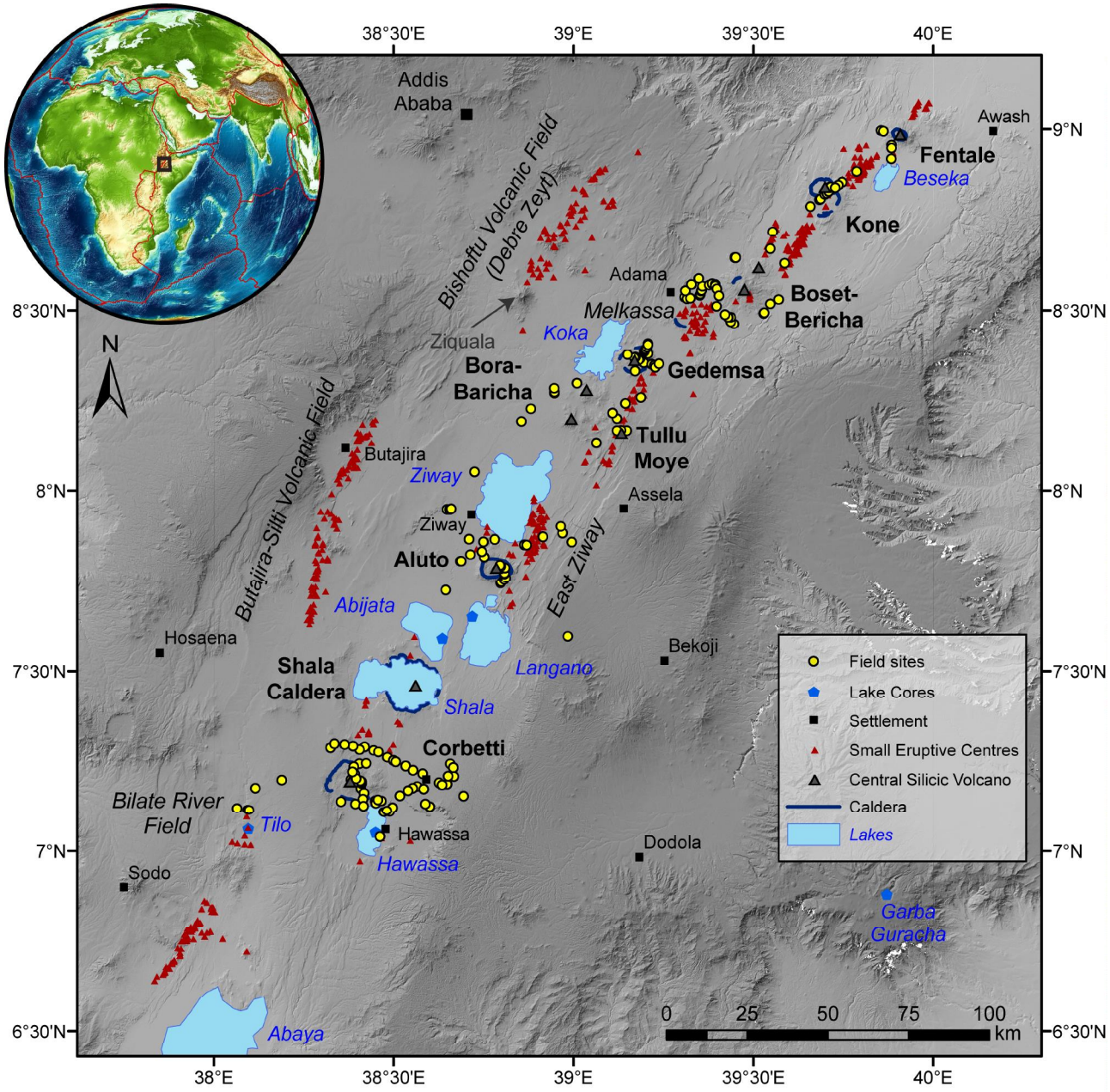
38°30'E
39°E
39°30'E
40°E
9°N
8°30'N
8°N
7°30'N
7°N
6°30'N
38°E
N
Addis Ababa
Awash
Fentale
Beseka
Kone
Bishoftu Volcanic Field (Debre Zeyt)
Adama
Boset-Bericha
Melkassa
Koka
Ziquala
Bora-Baricha
Gedemsa
Tullu Moye
Butajira
Butajira-Silti Volcanic Field
Ziway
Assela
Aluto
East Ziway
Abijata
Hosaena
Bekoji
Shala Caldera
Langano
Shala
Corbetti
Bilate River Field
Tilo
Hawassa
Dodola
Sodo
Garba Guracha
Abaya
Field sites
Lake Cores
Settlement
Small Eruptive Centres
Central Silicic Volcano
Caldera
Lakes
0
25
50
75
100
km

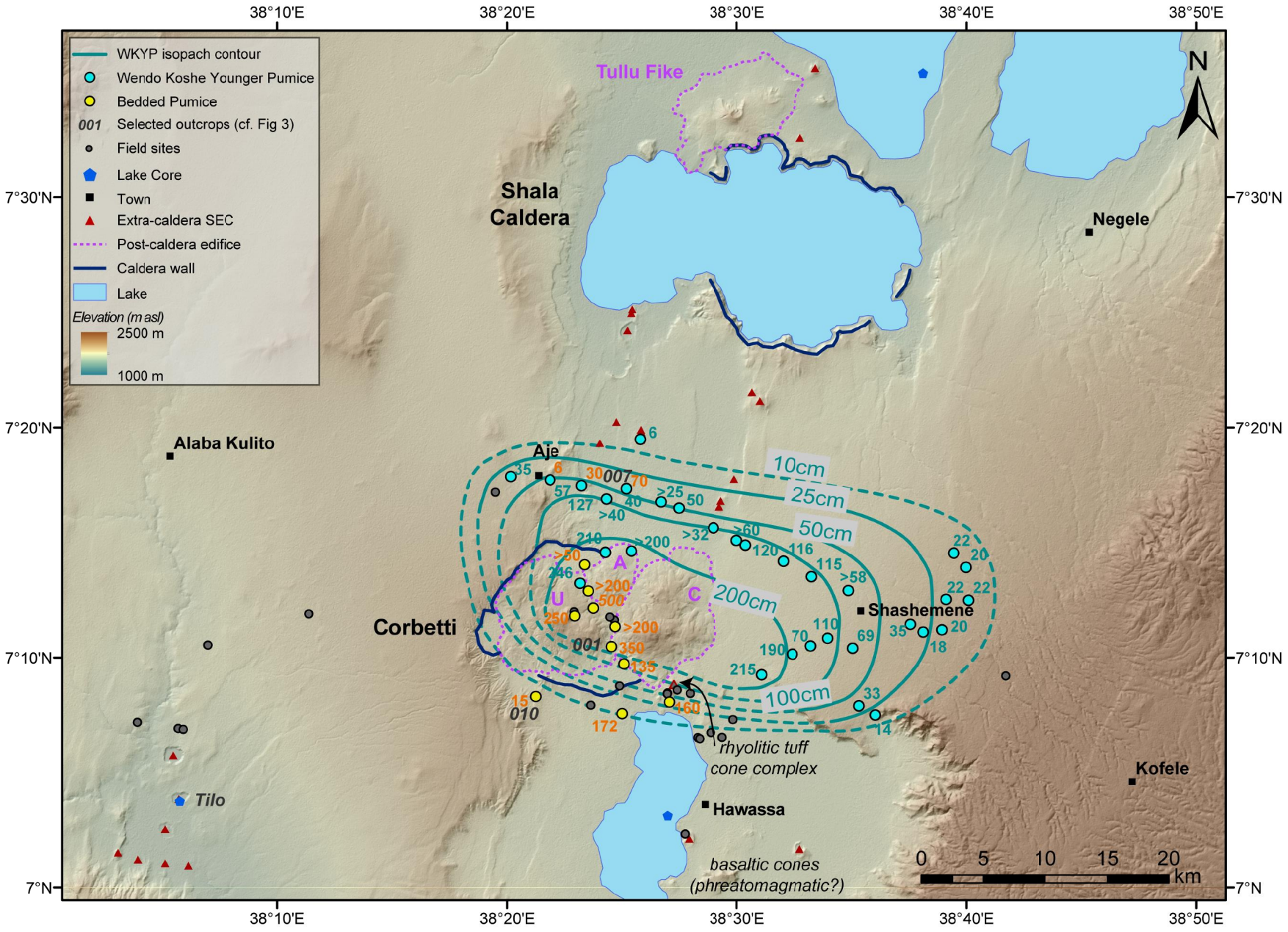
38°10'E
38°20'E
38°30'E
38°40'E
38°50'E
7°30'N
7°20'N
7°10'N
7°N
N
WKYP isopach contour
Wendo Koshe Younger Pumice
Bedded Pumice
001 Selected outcrops (cf. Fig 3)
Field sites
Lake Core
Town
Extra-caldera SEC
Post-caldera edifice
Caldera wall
Lake
Elevation (m asl)
2500 m
1000 m
Tullu Fike
Shala Caldera
Negele
Alaba Kulito
Aje
Corbetti
Shashemene
Tilo
Hawassa
Kofele
rhyolitic tuff cone complex
basaltic cones (phreatomagmatic?)
10cm
25cm
50cm
100cm
200cm
A
C
U
0 5 10 15 20 km

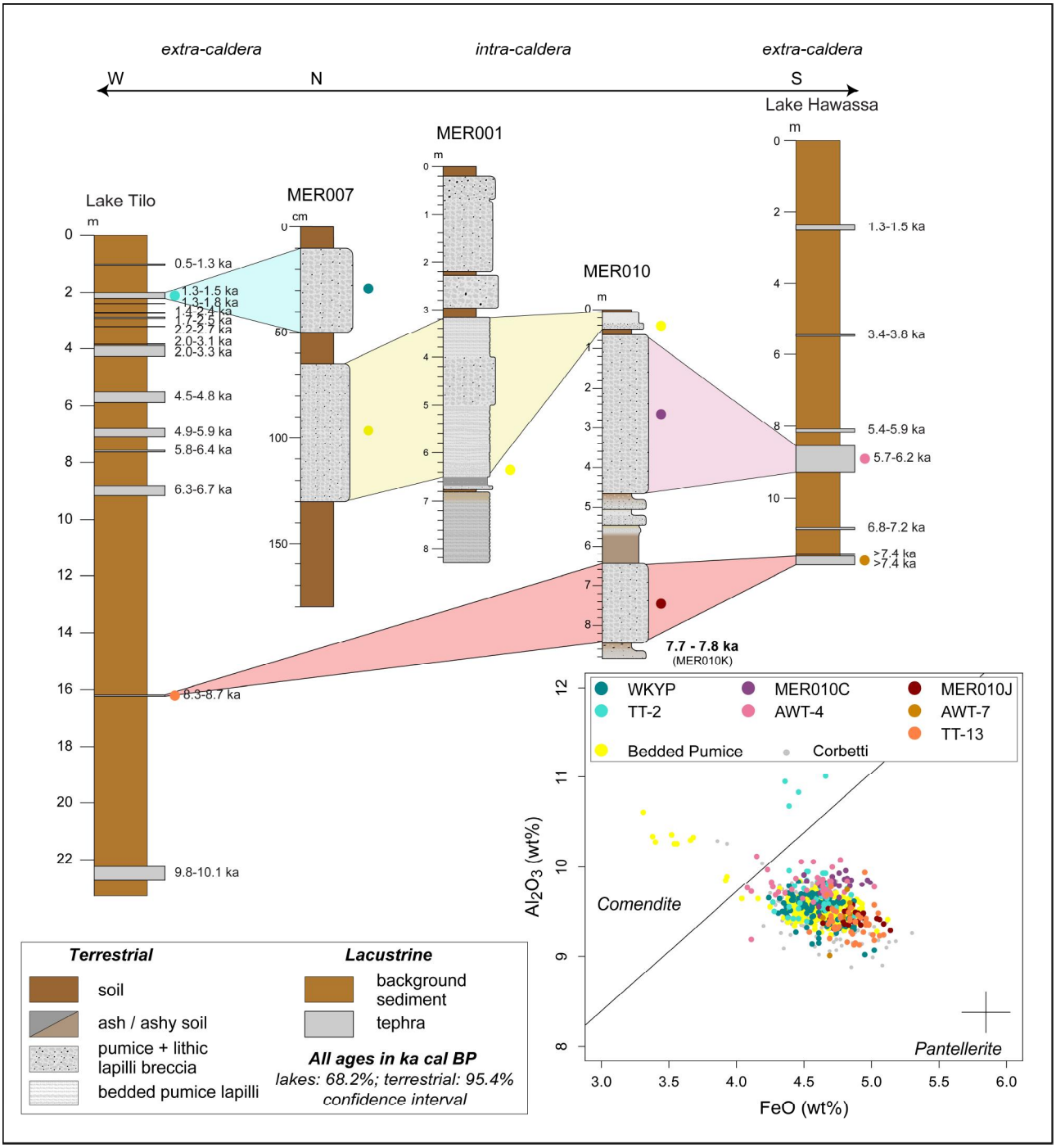
extra-caldera
intra-caldera
extra-caldera
W
N
S
Lake Hawassa
MER001
Lake Tilo
MER007
MER010
0.5-1.3 ka
1.3-1.5 ka
1.3-1.8 ka
1.4-2.4 ka
1.7-2.5 ka
2.2-2.7 ka
2.0-3.1 ka
2.0-3.3 ka
4.5-4.8 ka
4.9-5.9 ka
5.8-6.4 ka
6.3-6.7 ka
8.3-8.7 ka
9.8-10.1 ka
1.3-1.5 ka
3.4-3.8 ka
5.4-5.9 ka
5.7-6.2 ka
6.8-7.2 ka
>7.4 ka
>7.4 ka
7.7 - 7.8 ka
(MER010K)
Terrestrial
soil
ash / ashy soil
pumice + lithic lapilli breccia
bedded pumice lapilli
Lacustrine
background sediment
tephra
All ages in ka cal BP
lakes: 68.2%; terrestrial: 95.4% confidence interval
WKYP
TT-2
MER010C
AWT-4
MER010J
AWT-7
TT-13
Bedded Pumice
Corbetti
Comendite
Pantellerite
Al2O3 (wt%)
FeO (wt%)

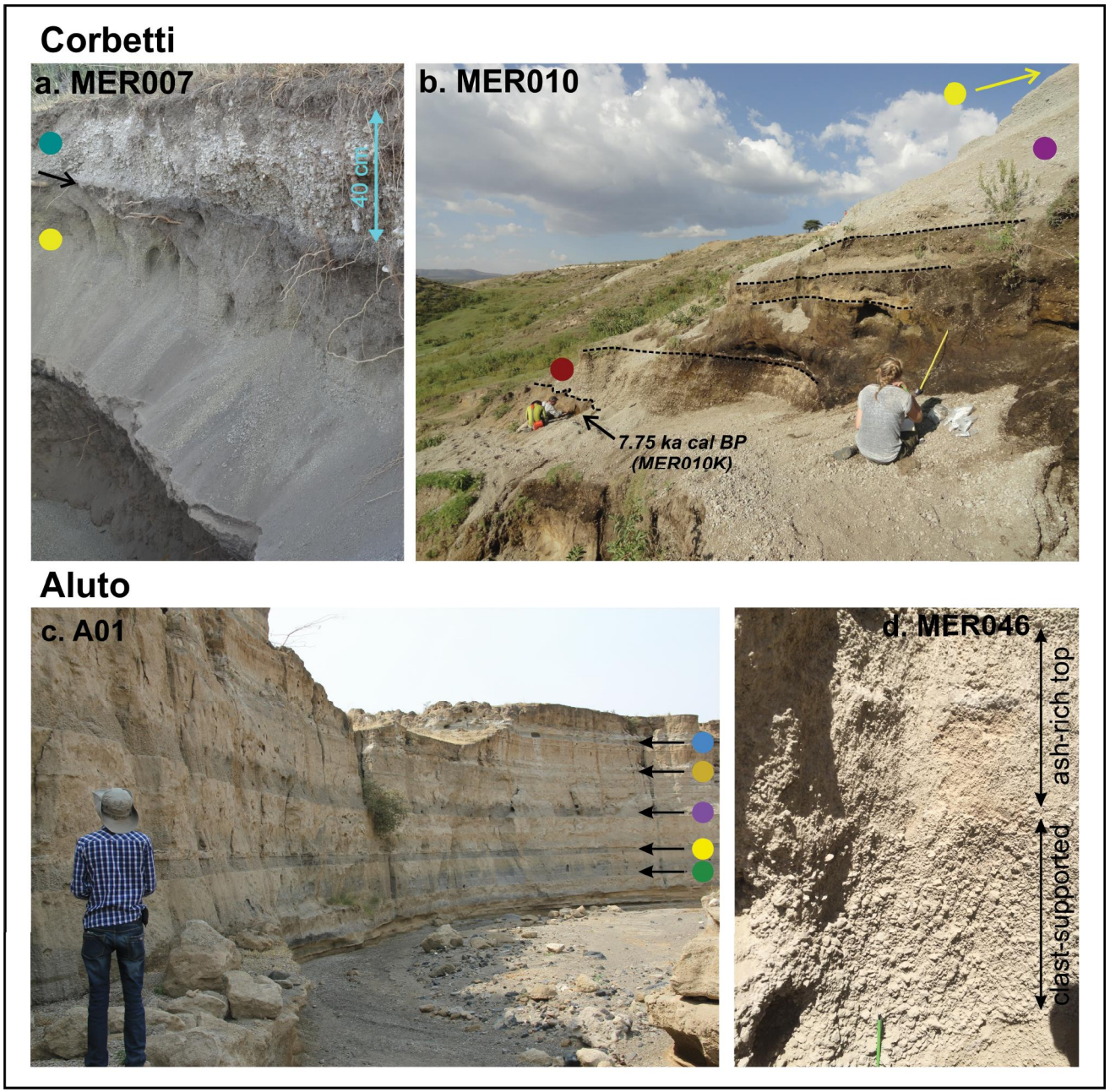
Corbetti
a. MER007
40 cm
b. MER010
7.75 ka cal BP
(MER010K)
Aluto
c. A01
d. MER046
ash-rich top
clast-supported

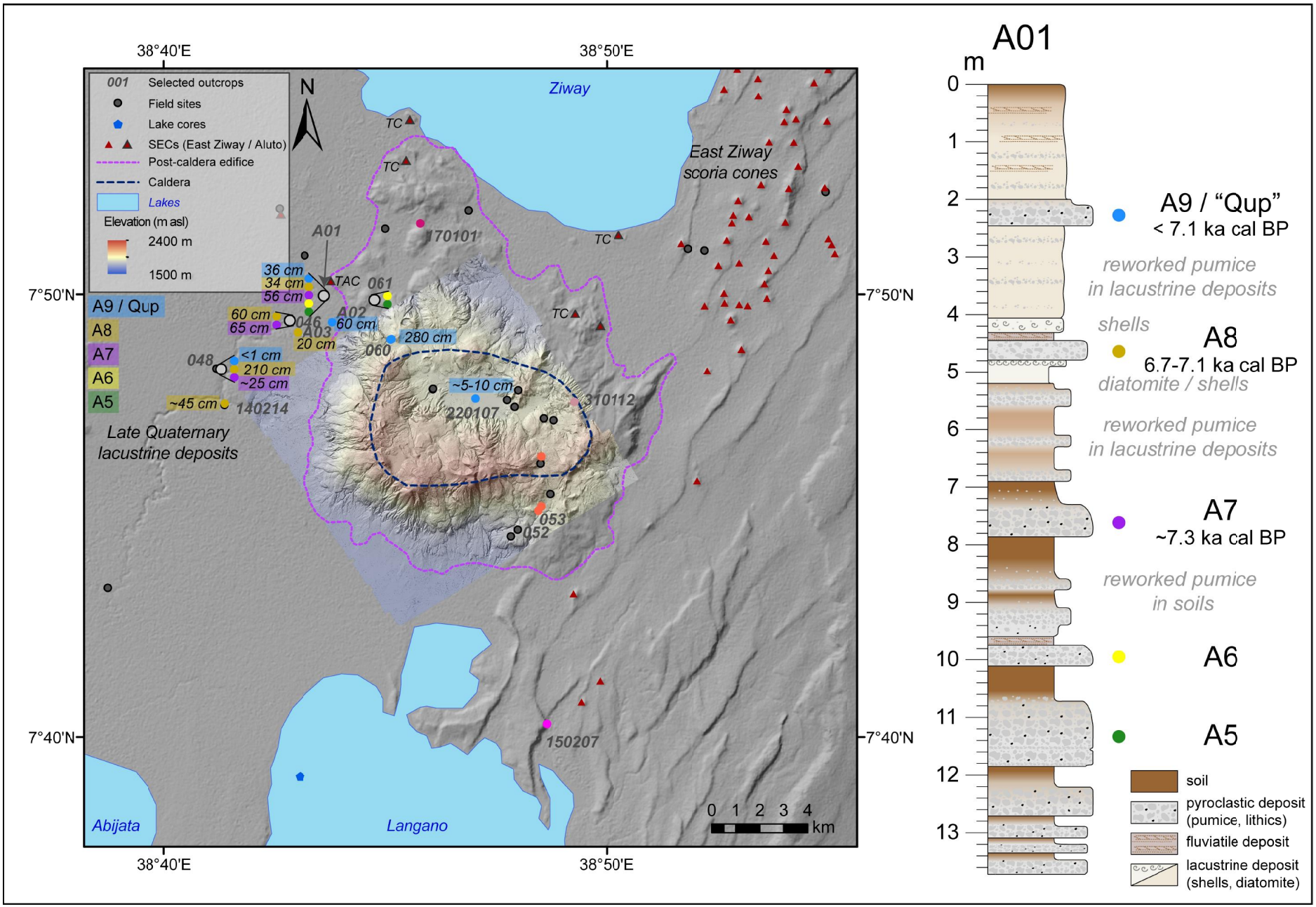
38°40'E
38°50'E
7°50'N
7°40'N
001 Selected outcrops
Field sites
Lake cores
SECs (East Ziway / Aluto)
Post-caldera edifice
Caldera
Lakes
Elevation (m asl)
2400 m
1500 m
N
Ziway
East Ziway scoria cones
TC
TAC
A01
A02
A03
170101
061
060
046
048
36 cm
34 cm
56 cm
60 cm
65 cm
60 cm
20 cm
280 cm
<1 cm
210 cm
~25 cm
~45 cm
140214
~5-10 cm
220107
310112
053
052
150207
A9 / Qup
A8
A7
A6
A5
Late Quaternary lacustrine deposits
Abijata
Langano
0 1 2 3 4 km
A01
m
0
1
2
3
4
5
6
7
8
9
10
11
12
13
A9 / "Qup"
< 7.1 ka cal BP
reworked pumice in lacustrine deposits
shells
A8
6.7-7.1 ka cal BP
diatomite / shells
reworked pumice in lacustrine deposits
A7
~7.3 ka cal BP
reworked pumice in soils
A6
A5
soil
pyroclastic deposit (pumice, lithics)
fluviatile deposit
lacustrine deposit (shells, diatomite)

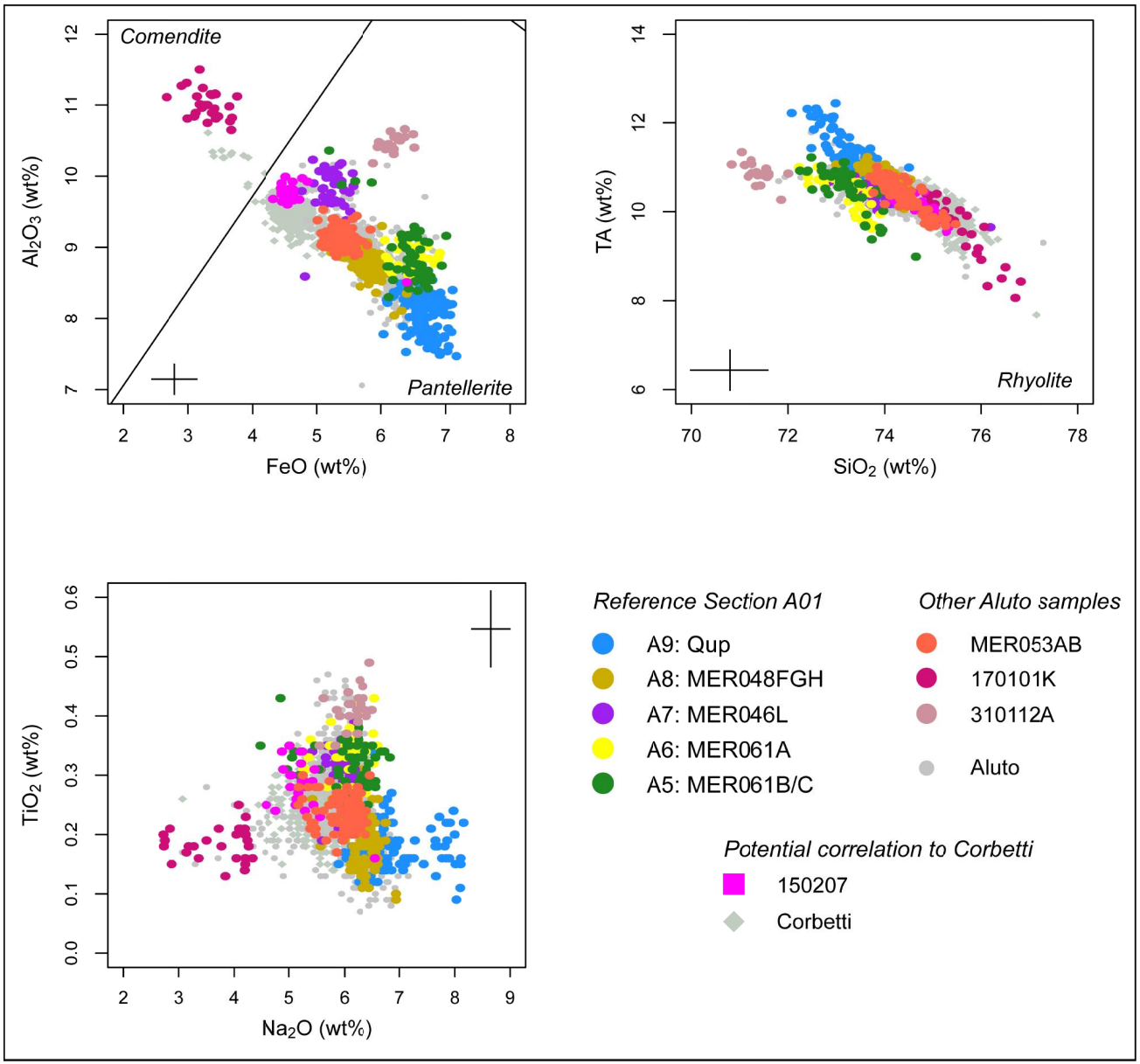
Comendite
Pantellerite
Al2O3 (wt%)
FeO (wt%)
Rhyolite
TA (wt%)
SiO2 (wt%)
TiO2 (wt%)
Na2O (wt%)
Reference Section A01
A9: Qup
A8: MER048FGH
A7: MER046L
A6: MER061A
A5: MER061B/C
Other Aluto samples
MER053AB
170101K
310112A
Aluto
Potential correlation to Corbetti
150207
Corbetti

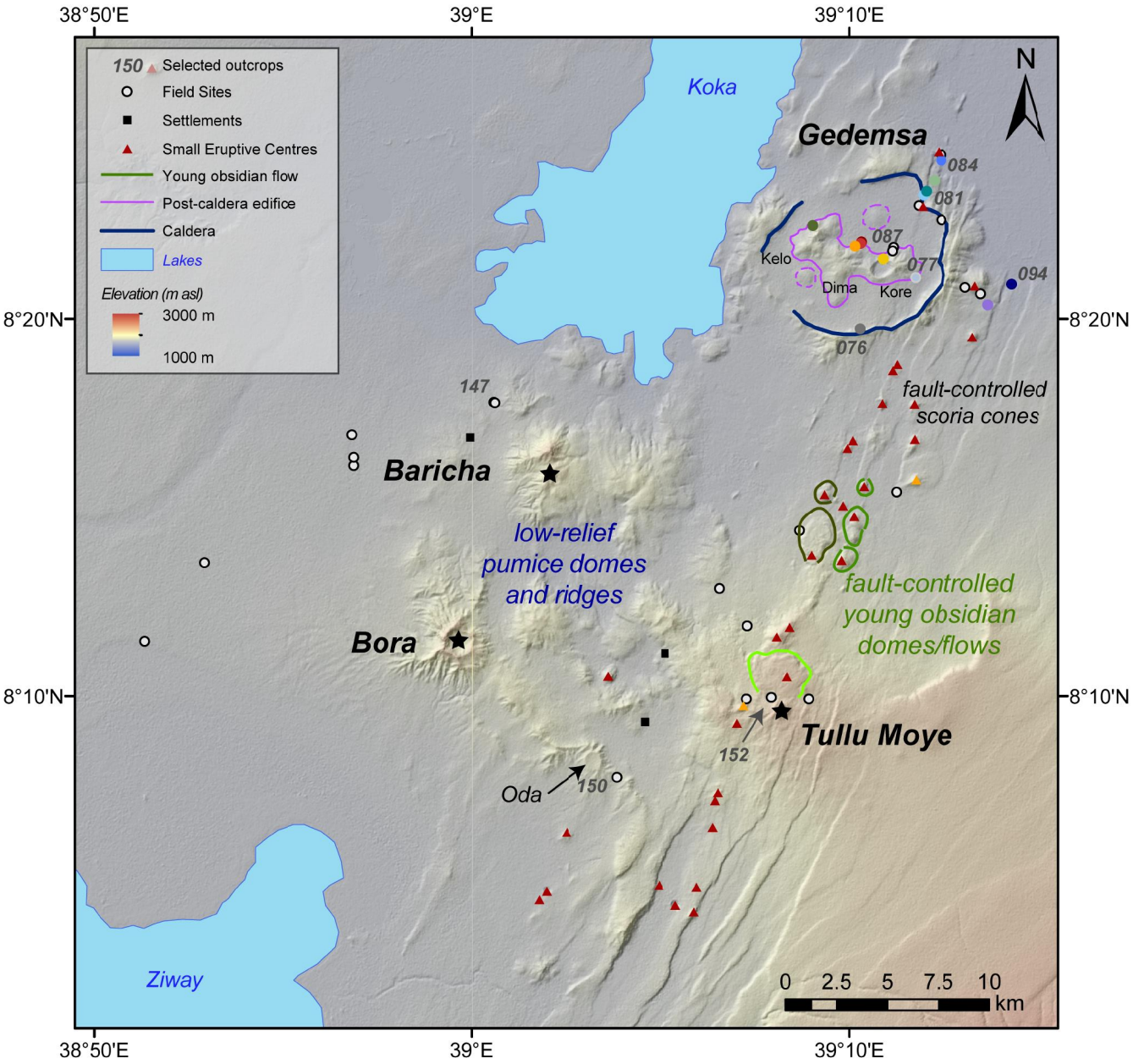
38°50'E
39°E
39°10'E
8°20'N
8°10'N
150 Selected outcrops
Field Sites
Settlements
Small Eruptive Centres
Young obsidian flow
Post-caldera edifice
Caldera
Lakes
Elevation (m asl)
3000 m
1000 m
Koka
Gedemsa
084
081
087
077
094
076
Kelo
Dima
Kore
N
147
Baricha
fault-controlled
scoria cones
low-relief
pumice domes
and ridges
fault-controlled
young obsidian
domes/flows
Bora
Tullu Moye
152
Oda
150
Ziway
0 2.5 5 7.5 10
km

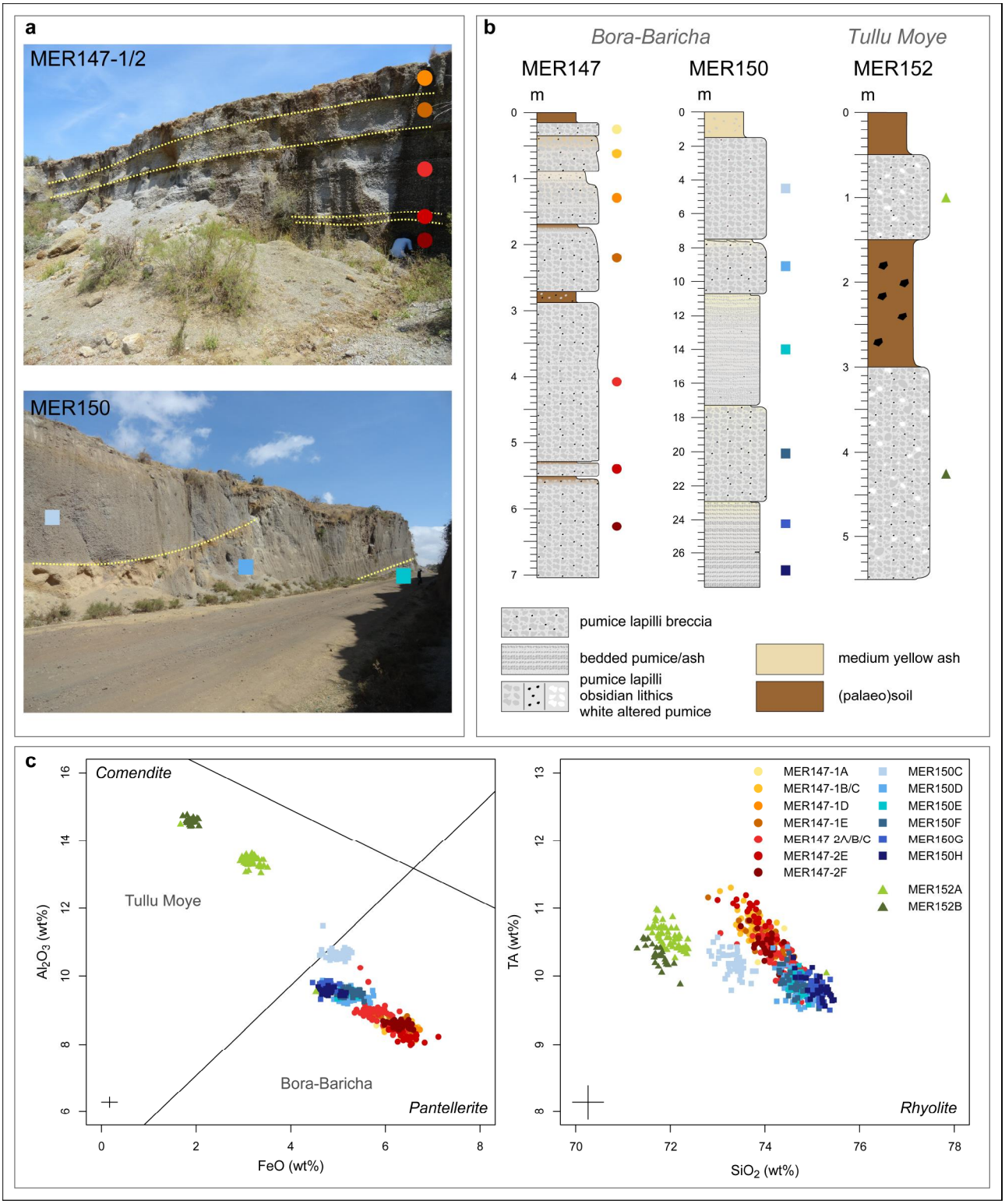
a
MER147-1/2
MER150
b
Bora-Baricha
Tullu Moye
MER147
MER150
MER152
m
pumice lapilli breccia
bedded pumice/ash
pumice lapilli
obsidian lithics
white altered pumice
medium yellow ash
(palaeo)soil
c
Comendite
Tullu Moye
Bora-Baricha
Pantellerite
Al2O3 (wt%)
FeO (wt%)
MER147-1A
MER147-1B/C
MER147-1D
MER147-1E
MER147 2A/B/C
MER147-2E
MER147-2F
MER150C
MER150D
MER150E
MER150F
MER150G
MER150H
MER152A
MER152B
TA (wt%)
SiO2 (wt%)
Rhyolite

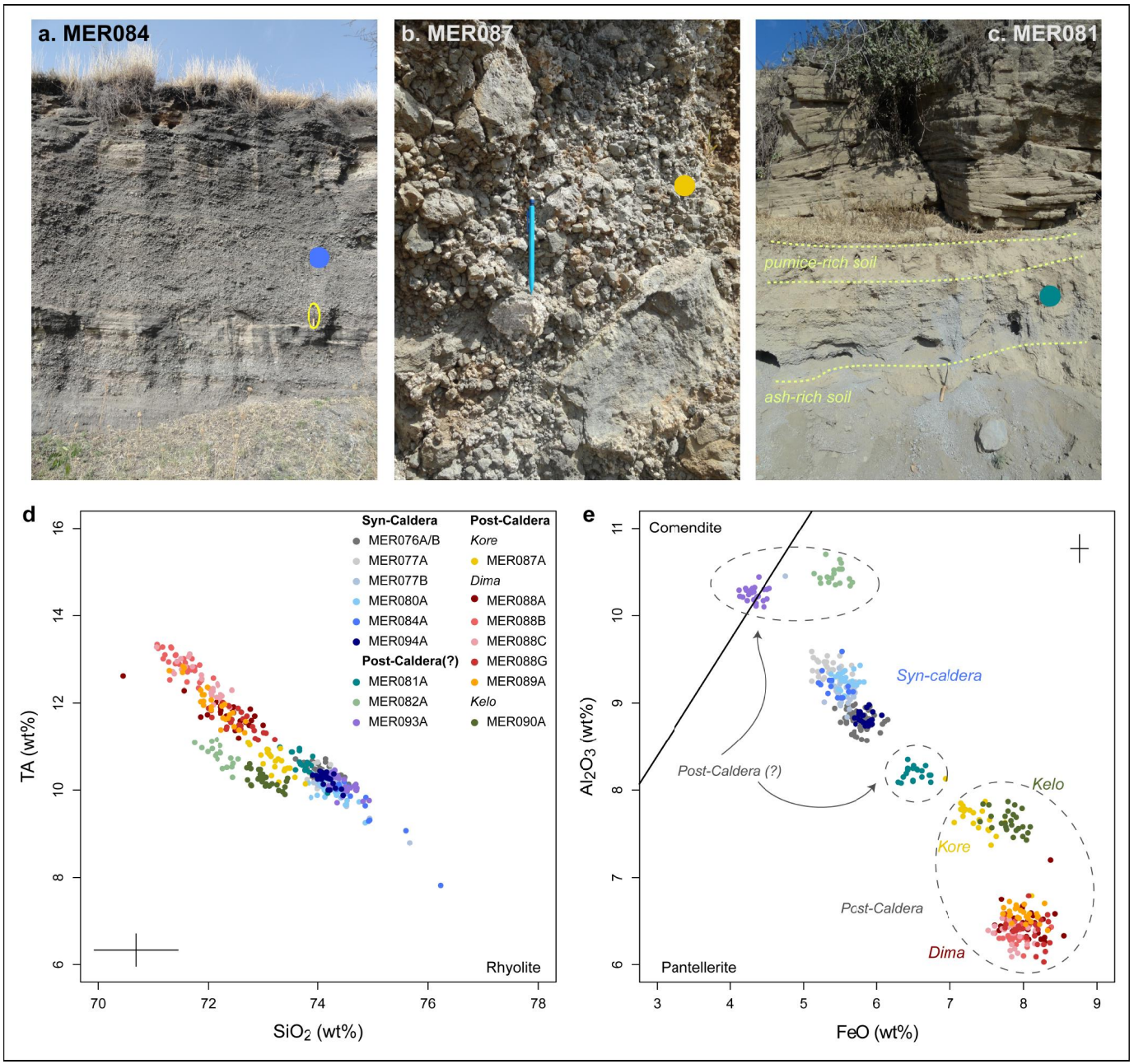
a. MER084
b. MER087
c. MER081
pumice-rich soil
ash-rich soil
d
Syn-Caldera
MER076A/B
MER077A
MER077B
MER080A
MER084A
MER094A
Post-Caldera(?)
MER081A
MER082A
MER093A
Post-Caldera
Kore
MER087A
Dima
MER088A
MER088B
MER088C
MER088G
MER089A
Kelo
MER090A
Rhyolite
TA (wt%)
SiO2 (wt%)
e
Comendite
Pantellerite
Syn-caldera
Post-Caldera (?)
Kelo
Kore
Pcst-Caldera
Dima
Al2O3 (wt%)
FeO (wt%)

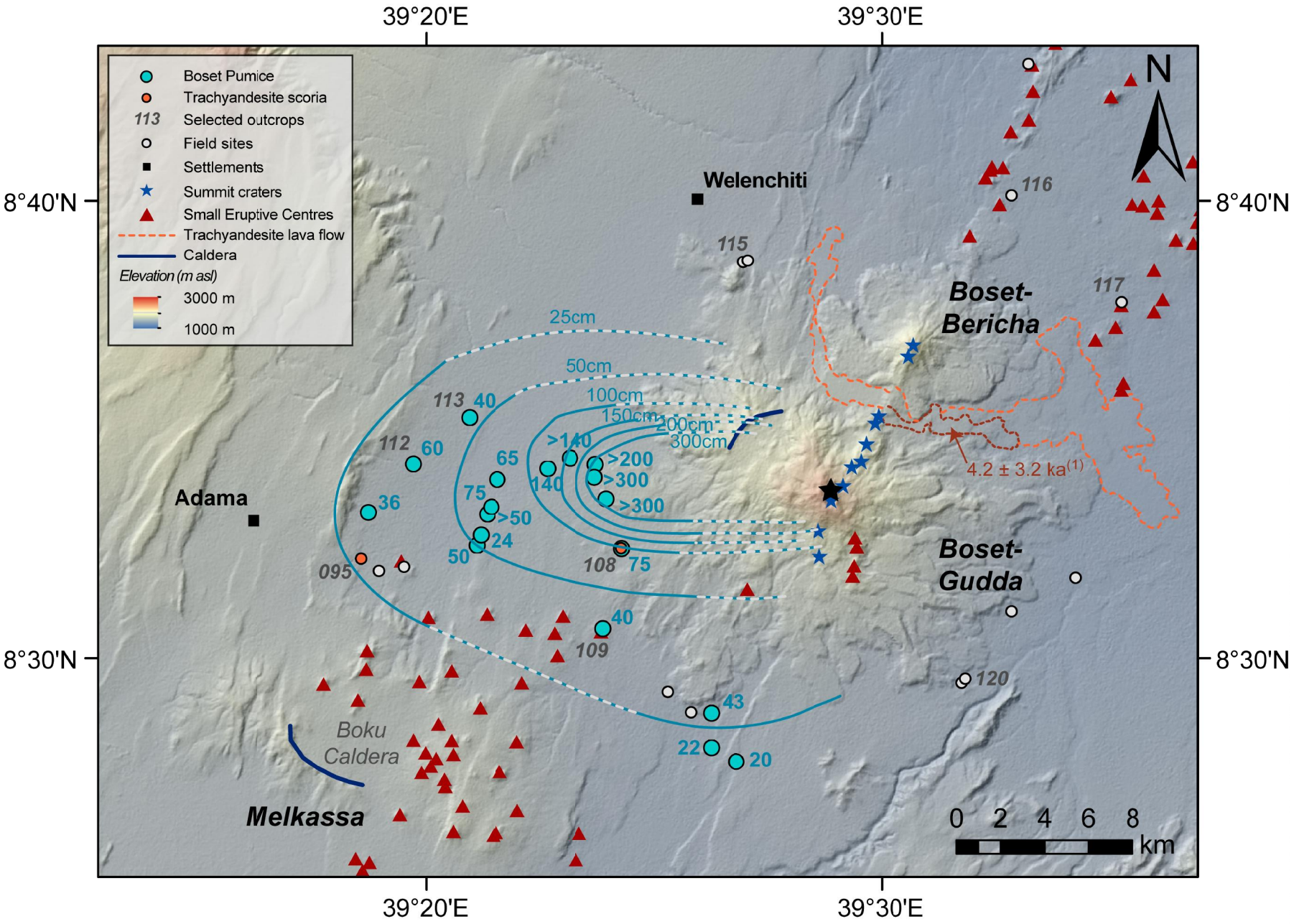
39°20'E
39°30'E
8°40'N
8°30'N
N
Boset Pumice
Trachyandesite scoria
113 Selected outcrops
Field sites
Settlements
Summit craters
Small Eruptive Centres
Trachyandesite lava flow
Caldera
Elevation (m asl)
3000 m
1000 m
Welenchiti
Adama
Melkassa
Boku Caldera
Boset-Bericha
Boset-Gudda
115
116
117
120
095
108
109
25cm
50cm
100cm
150cm
200cm
300cm
113 40
112 60
65
>140
>200
>300
>300
75
140
36
>50
24
50
75
40
43
22
20
4.2 ± 3.2 ka(1)
0 2 4 6 8
km

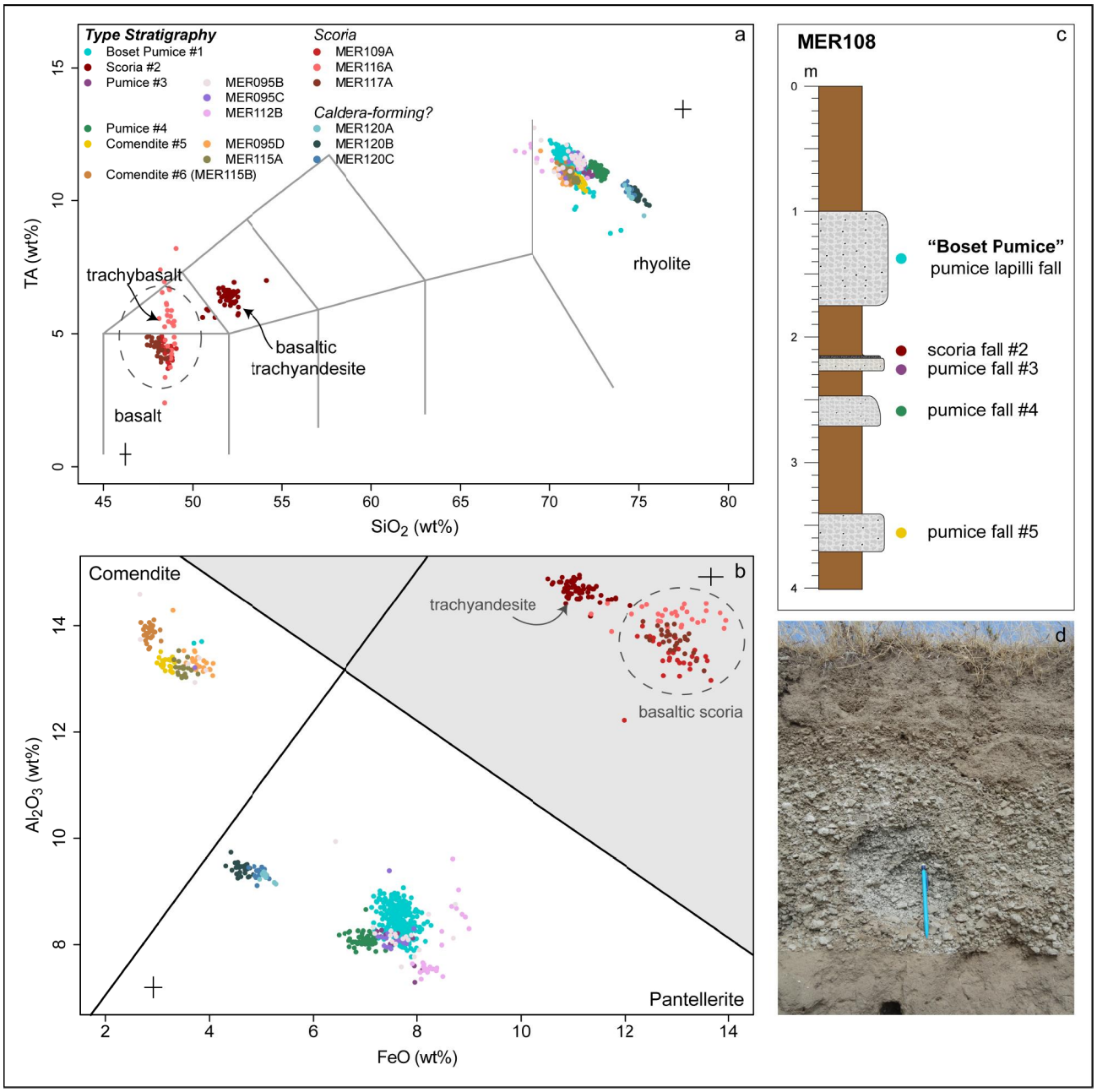
a
Type Stratigraphy
Boset Pumice #1
Scoria #2
Pumice #3
Pumice #4
Comendite #5
Comendite #6 (MER115B)
MER095B
MER095C
MER112B
MER095D
MER115A
Scoria
MER109A
MER116A
MER117A
Caldera-forming?
MER120A
MER120B
MER120C
trachybasalt
basaltic trachyandesite
basalt
rhyolite
TA (wt%)
SiO2 (wt%)
b
Comendite
trachyandesite
basaltic scoria
Pantellerite
Al2O3 (wt%)
FeO (wt%)
c
MER108
m
"Boset Pumice" pumice lapilli fall
scoria fall #2
pumice fall #3
pumice fall #4
pumice fall #5
d

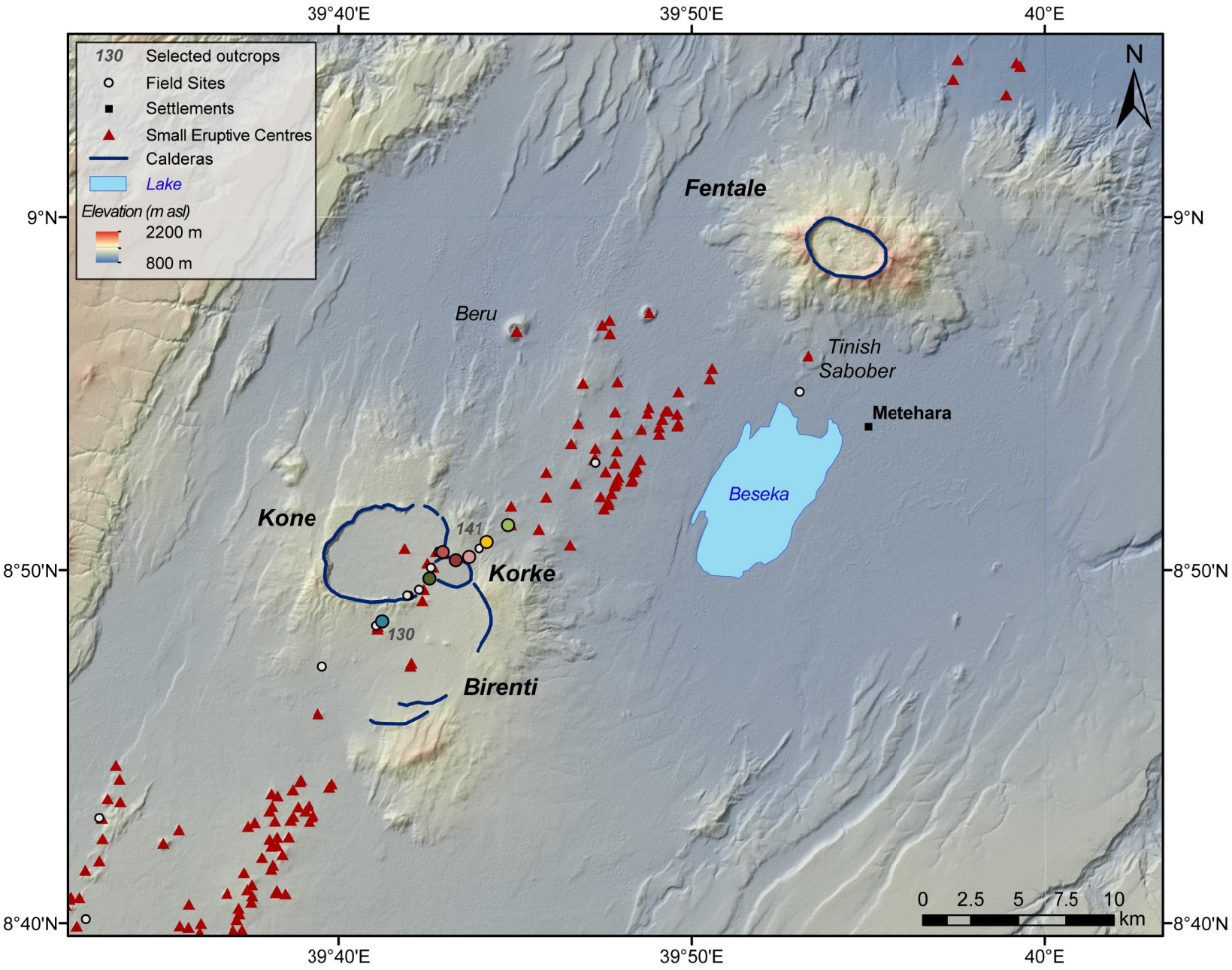
130 Selected outcrops
Field Sites
Settlements
Small Eruptive Centres
Calderas
Lake
Elevation (m asl)
2200 m
800 m
39°40'E
39°50'E
40°E
9°N
8°50'N
8°40'N
N
Fentale
Beru
Tinish
Sabober
Metehara
Beseka
Kone
141
Korke
130
Birenti
0 2.5 5 7.5 10
km

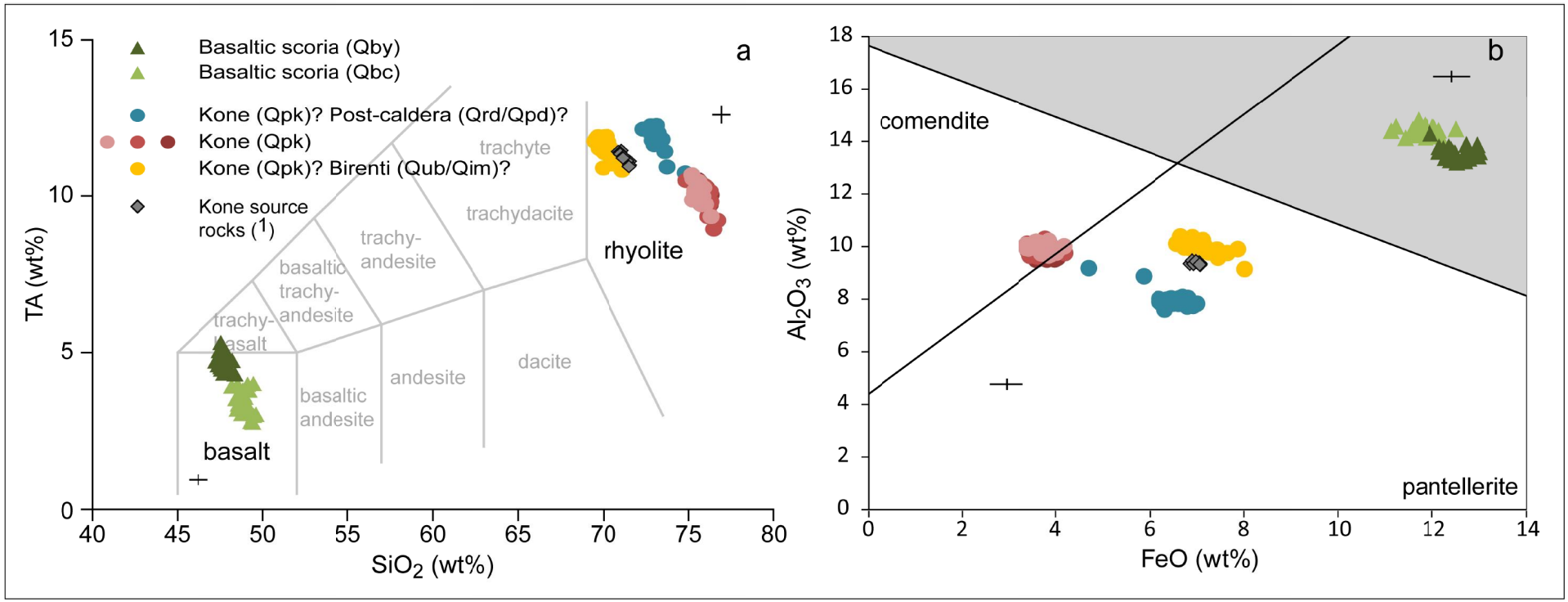
a
Basaltic scoria (Qby)
Basaltic scoria (Qbc)
Kone (Qpk)? Post-caldera (Qrd/Qpd)?
Kone (Qpk)
Kone (Qpk)? Birenti (Qub/Qim)?
Kone source rocks ([1])
trachyte
trachydacite
trachy-andesite
basaltic trachy-andesite
trachy-basalt
andesite
dacite
basaltic andesite
rhyolite
basalt
TA (wt%)
SiO2 (wt%)
b
comendite
pantellerite
Al2O3 (wt%)
FeO (wt%)

Corbetti

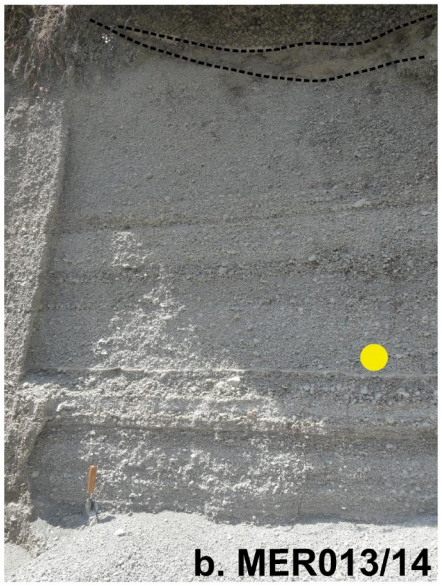

Aluto